Title
Measurement of Ultrafast Laser Pulses Produced via Second-Harmonic Generation in ZnSe/S

Author
Izarraraz, Alberto

Publication Date
2022

Peer reviewed|Thesis/dissertation

Measurement of Ultrafast Laser Pulses
Produced via Second-Harmonic Generation in ZnSe/S

By

ALBERTO IZARRAZ
THESIS

Submitted in partial satisfaction of the requirements for the degree of

MASTER OF SCIENCE

in

Electrical and Computer Engineering

in the

OFFICE OF GRADUATE STUDIES

of the

UNIVERSITY OF CALIFORNIA

DAVIS

Approved:

_____
William Putnam, Chair

_____
Diego Yankelevich

_____
Juan Sebastian Gomez-

Diaz Committee in Charge

2022

Measurement of Ultrafast Laser Pulses

Produced via Second-Harmonic Generation in ZnSe/S

by

Alberto Izarraraz

Submitted to the Department of Electrical and Computer Engineering
on November 14, 2022, in partial fulfillment of the
requirements for the degree of
Master of Science in Electrical Engineering

Abstract

Ultrafast laser systems based on Cr-doped ZnSe/S gain media can provide powerful, flexible laser light in the mid-infrared. Beyond their mid-infrared output, Cr:ZnSe/S lasers often possess a second-harmonic output. Second harmonic is naturally generated via random quasi-phasematching (RQPM) in polycrystalline ZnSe/S when driven by infrared light. In Cr:ZnSe/S lasers, this second-harmonic generation (SHG) can often reach powers comparable to the output powers of conventional pulsed laser systems, on the order of hundreds of milliwatts. Although interesting, there has been limited experimental investigation into this naturally generated SHG. In this thesis, we tackle the problem of measuring these SHG pulses. The measurement of these ultrafast pulses requires an understanding of nonlinear optical interactions as well as the development of both precision electronics and optics. In this thesis, background is provided on the nonlinear interactions that lead to SHG as well as the techniques and instrumentation necessary to measure ultrafast pulses. Additionally, the development of high-gain, low-noise transimpedance amplifiers for pulse measurement is described. Furthermore, a precision optical system for the measurement of SHG pulses from a Cr:ZnSe/S laser is presented and initial measurement results are discussed.

Thesis Supervisor: William Putnam
Title: Assistant Professor

Acknowledgments

Dedicated to

Miguel Izarraraz, my father.

Here is to a man that does not falter when the going gets tough. A man that always gives without ever asking. A father that always seeks to understand rather than blatantly contesting your opinions. And a Dad that has taught me how to think, and not telling me what to think. A man who takes pride in his work, yet remains humble once the work is done. Your guidance and support have made this all possible.

I also want to thank Marissa, my mother. Who stands as tall as my dad, even though her driver's license says otherwise. She always believes in me, even when I don't believe in myself. Even at the doorstep of failure, she would pat me on the back and say, 'se que lo lograras'. (I know you can make it). I also want to give thanks to my siblings, who have taught countless lessons as most of my learning growing up was through the experiences of my older siblings.

I shout out to my colleagues, Trevor Pollack and Alexander Gardner. From countless of hours studying together, to more countless hours taking needed breaks in downtown Davis. The intellectual support they have provided is what made coming back to school an easy transition.

To my major professor, William Putnam. Your talent to explain complex concept and ideas together with your bottomless amounts of patience has saved me countless of times from selling my textbooks and calling it quits. I am truly grateful that I had an opportunity to have you as a mentor for these past couple of years.

And finally, to the person I had to save for last in fear of forgetting about everyone else, my dear wife Stephanie. The amount of support you have shown and the unconditional love that you have blessed me with truly knows no bounds. I will always strive to be the greatest husband you deserve.

Contents

List of Figures

Chapter 1

Introduction

The primary goal of this thesis is to measure ultrafast laser pulses produced via second-harmonic generation in ZnSe/S crystals. Specifically, we aim to develop the necessary components and systems to measure the duration of short pulses produced in this second-harmonic generation process. To make these measurements, precision electronics and optics will be necessary. In this thesis, we will describe the design, implementation, and testing of a high-gain, low-noise transimpedance amplifier. This amplifier is capable of amplifying weak currents produced by weak optical signals in photodiodes. These weak optical signals come from our ultrafast pulse measurement system. We will describe the construction of an initial measurement system, an interferometric autocorrelator. We will discuss our initial measurements with this system, and we will overview the limitations of the system and our next steps. Before diving into the details of the precision electronic and optical instruments constructed, we provide an overview, in this chapter, of the optical system of interest: a Cr-doped ZnSe/S laser system. As we will discuss, this mid-infrared laser system naturally produces a strong second harmonic in its gain crystal. This is the second harmonic that we aim to characterize. After describing our core laser system, we will provide a brief overview of the scope and direction of the rest of this thesis.

1.1 Cr:ZnSe/S Mid-Infrared Lasers

The central goal of this thesis centers around a specific mid-infrared laser system. The mid-infrared portion of the electromagnetic spectrum includes electromagnetic waves with wavelengths from around 2 μm to 20 μm. This portion of the spectrum is of particular interest for spectroscopy, since in this so-called "molecular fingerprint" region, nearly every molecule exhibits rotational or vibrational resonances. Although very interesting for spectroscopic applications, there are few coherent sources in the mid-infrared.

In recent years, ultrafast laser systems based on Cr-doped ZnSe/S gain media have emerged as an exciting option for coherent, powerful mid-infrared light [1]. The basic structure of one of these laser systems in illustrated in Figure 1-1.

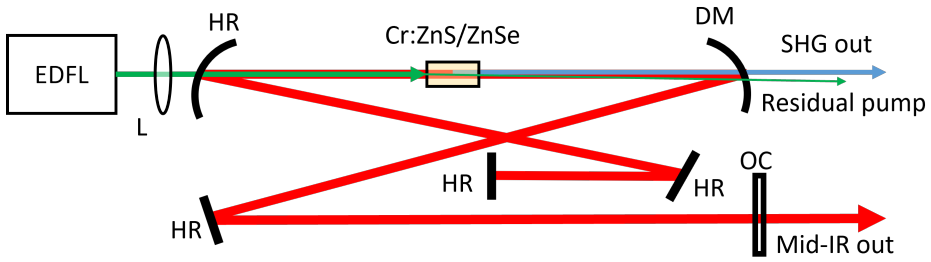

Figure 1-1: **Cr:ZnSe/S Laser**. HR: high reflector; L: lens. (Other acronyms in text.)

The Cr:ZnSe/S laser is a Kerr-lens modelocked (KLM) solid-state laser. In the Ultrafast Nonlinear Optics (UNO) group at the University of California, Davis, we have a CLPF Series Cr:ZnSe/S laser manufactured by IPG Photonics Inc. The following overview of Cr:ZnSe/S lasers primarily associates with the specifications of our system. As shown in Figure 1-1, the Cr:ZnSe/S polycrystalline gain element is pumped using erbium-doped fiber lasers (EDFLs) operating at 1530-1570 nm. The gain element in our Cr:ZnSe/S laser system is antireflection-coated (AR-coated) and the pump laser is normally incident to maximize pump and laser intensity inside the gain element. (Additionally, this further increases the the likelihood of nonlinear effects in the crystal.) The mid-infrared output of the laser exits through the output coupler (OC).

The output of the Cr:ZnSe/S laser can vary, but typically the output is around 2.4 μm in center wavelength with a pulse duration down to around 30 fs. The pulse repetition rate

is 80.97 MHz, pulse energy is 40 nJ, and the time-bandwidth product is <0.35. The overall optical power of the system is 3.2 W for the fundamental mid-infrared pulse.

Beyond the mid-infrared output, the Cr:ZnSe/S laser also possesses a second-harmonic output. As will be described in the next chapter, the grain size and polycrystalline nature of the ZnSe/S gain crystal naturally enable random quasi-phasematching (RQPM) and strong second-harmonic generation (SHG). In our laser system, a dichroic mirror (DM) is used to out-couple the SHG. The SHG output power is around 250 mW, and the spectrum ranges from around 1000-1250 nm.

Preliminary measurements by other researchers have indicated that the RQPM SHG might create pulses ∼100-200 fs in duration [2] [3]. Additionally, the bandwidth of the SHG suggests that even shorter pulses might be possible. In this thesis, we aim to develop the necessary components and systems to measure the duration of these SHG pulses from our Cr:ZnSe/S laser system.

1.2 Outline of This Thesis

In this thesis, we tackle the problem of measuring near-infrared pulses produced via second harmonic generation in a ZnSe/S crystal. The measurement of these ultrafast pulses requires an understanding of nonlinear optical interactions as well as the development of both precision electronics and optics. In Chapter 2, we provide background on the nonlinear optical interactions that lead to the SHG of interest as well as the effects necessary to measure these SHG pulses. Additionally, we overview our initial pulse characterization strategy: autocorrelation. In Chapter 3, we describe the precision electronics that we have developed for measuring these SHG pulses. Specifically, we describe the design, implementation, and testing of a high-gain, low-noise transimpedance amplifier. Lastly, in Chapter 4, we describe the optical arrangement for our pulse measurement. We describe the construction and alignment of an interferometric autocorrelator, and we present our initial results. Finally, in Chapter 4, we discuss the limitations of our initial autocorrelator and describe the next steps for this project.

Chapter 2

Background

In this chapter, we provide essential background on nonlinear optics [4] and ultrafast pulse measurement [5]. The first two sections of this chapter will focus on concepts in nonlinear optics that relate to the aims of this thesis. We begin our review by revisiting the wave equation for linear, homogeneous, and isotropic media. We then explore nonlinear media and show that nonlinear polarization can drive our familiar electromagnetic wave equation and produce harmonics. Next, we provide a brief overview of how nonlinear processes are controlled and optimized through phasematching, and we describe the releveant phasematching processes for the work in this thesis. In the last section of this chapter, we overview ultrafast pulse measurement. Specifically, the technique that allows us to measure the aforementioned second harmonic pulses is explained. To provide intuition, we being this section with a discussion of an autocorrelator that only uses linear components. Then, we introduce nonlinearity and describe intensity autocorrelation and an interferometric autocorrelation. Sample pulses and calculations are used to explain the limitations of each techniques.

2.1 Nonlinear Optics

Nonlinear optics corrected the wrongs of past statements that were once thought of as facts. It was previously thought that the refractive index of a material did not depend on light intensity, the frequency of light was never altered when passing through a medium, and that light could not control light. In fact,the many elements in this universe allow the existence

of a vast array of materials, each with their own characteristics. In optics, materials can be made to exhibit linear or nonlinear effects, depending on their composition and configuration.

To describe linear and nonlinear effects in optics, we consider the constitutive relation between the electric field $\mathbf{E}$ and the electric displacement field $\mathbf{D}$. For homogeneous and isotropic dielectric materials, this relation can be described as:

$$\mathbf{D} = \epsilon\, \mathbf{E} \tag{2.1}$$

The permittivity of a material can also be described in terms of the material's electric susceptibility (χ), where $\epsilon_0 = 8.854 \times 10^{-12}$ F/m.

$$\epsilon = \epsilon_0(1 + \chi) \tag{2.2}$$

Equation 2.1 appears linear at first. However, in general, a material's permittivity (ϵ) is itself a function of the electric field $\mathbf{E}$:

$$\epsilon(\mathbf{E}) = \epsilon_0(1 + \chi^{(1)} + \chi^{(2)}\mathbf{E} + \chi^{(3)}\mathbf{E}^2 + \dots) \tag{2.3}$$

In the above expansion, the higher order terms are generally insignificant; this makes materials generally linear. However, with a high enough magnitude in the electric field, nonlinear effects become apparent.

An interesting result of nonlinear effects, and a main point in this thesis, is the generation of harmonics. This can be shown by allowing $\mathbf{E} = E_0 e^{j\omega t}$. (We temporarily ignore the vector nature of the electric field.) Using Equation 2.1 and Equation 2.3, we can write:

$$
\begin{aligned}
\mathbf{D} &= \epsilon(\mathbf{E})\mathbf{E} \\
&= \left(\epsilon_0(1 + \chi^{(1)} + \chi^{(2)}\mathbf{E} + \chi^{(3)}\mathbf{E}^2 + \dots)\right)\mathbf{E} \\
&= \left(\epsilon_0 + \epsilon_0\chi^{(1)} + \epsilon_0\chi^{(2)}\mathbf{E} + \epsilon_0\chi^{(3)}\mathbf{E}^2 + \dots\right)\mathbf{E} \\
&= \epsilon_0\mathbf{E} + \epsilon_0\chi^{(1)}\mathbf{E} + \epsilon_0\chi^{(2)}\mathbf{E}^2 + \epsilon_0\chi^{(3)}\mathbf{E}^3 + \dots \\
&= \epsilon_0 E_0 e^{j\omega t} + \epsilon_0\chi^{(1)} E_0 e^{j\omega t} + \epsilon_0\chi^{(2)}(E_0 e^{j\omega t})^2 + \epsilon_0\chi^{(3)}(E_0 e^{j\omega t})^3 + \dots \\
&= \epsilon_0 E_0 e^{j\omega t} + \epsilon_0\chi^{(1)} E_0 e^{j\omega t} + \epsilon_0\chi^{(2)} E_0^2 e^{2j\omega t} + \epsilon_0\chi^{(3)} E_0^3 e^{3j\omega t} + \dots
\end{aligned} \tag{2.4}
$$

From the above analysis, we see that in a crystal with a high enough $\chi^{(2)}$ susceptibility and a high electric field, a second harmonic can be generated. This is the origin of the generated second harmonic pulse in our Cr:ZnSe/S laser that we plan to measure.

Reverting Equation 2.4 back to an arbitrary $\mathbf{E}$ field will allow us to describe the above in a more suitable manner, via nonlinear polarization. Specifically, in Equation 2.5, lets split the first-order, linear portion of the $\mathbf{D}$ field, with the higher-order, nonlinear parts:

$$
\begin{aligned}
\mathbf{D} &= \epsilon_0 E_0 e^{j\omega t} + \epsilon_0\chi^{(1)} E_0 e^{j\omega t} + \epsilon_0\chi^{(2)} E_0^2 e^{2j\omega t} + \epsilon_0\chi^{(3)} E_0^3 e^{3j\omega t} + \dots \\
&= \epsilon_0\mathbf{E} + \epsilon_0\chi^{(1)}\mathbf{E} + \epsilon_0\chi^{(2)}\mathbf{E}^2 + \epsilon_0\chi^{(3)}\mathbf{E}^3 + \dots \\
&= \epsilon_0\mathbf{E} + \epsilon_0\chi^{(1)}\mathbf{E} + \mathbf{P_{NL}} \\
&= \epsilon^{(1)}\mathbf{E} + \mathbf{P_{NL}}
\end{aligned} \tag{2.5}
$$

Polarization is the dipole moment per unit volume, and as we see in the above, the polarization will depend on both the linear and nonlinear effects due to the applied optical field. In conventional linear optics, polarization drives the well-known wave equation:

$$
\nabla^2\mathbf{E} - \frac{\epsilon^{(1)}}{c^2}\frac{\partial^2\mathbf{E}}{\partial t^2} = 0
$$

In this equation, the polarization results in the refractive index, $\sqrt{\epsilon^{(1)}}$. With our understanding of nonlinear polarization, $\mathbf{P_{NL}}$, we now aim to derive a nonlinear wave equation that can

describe the dynamic generation of harmonics in a nonlinear material. Towards this end, let us begin by listing the necessary equations for our derivation:

$$\nabla \times \mathbf{E} = -\frac{\partial \mathbf{B}}{\partial t} \qquad \textit{Faraday's Law of Induction} \tag{2.6}$$

$$\nabla \times \mathbf{H} = \frac{\partial \mathbf{D}}{\partial t} \qquad \textit{Source-free Ampere's Law} \tag{2.7}$$

$$\nabla \times (\nabla \times \mathbf{E}) = \nabla(\nabla \cdot \mathbf{E}) - \nabla^2 \mathbf{E} \qquad \textit{Vector Identity} \tag{2.8}$$

$$\nabla \cdot \mathbf{D} = 0 \qquad \textit{Source-free Gauss' Law} \tag{2.9}$$

$$\mathbf{B} = \mu_0 \mathbf{H} \qquad \textit{Constitutive Relation} \tag{2.10}$$

Starting with Equation 2.6, we can plug in Equation 2.10 and take the curl of both sides:

$$\nabla \times \mathbf{E} = -\frac{\partial \mathbf{B}}{\partial t}$$
$$\nabla \times (\nabla \times \mathbf{E}) = \nabla \times \left(-\mu_0 \frac{\partial \mathbf{H}}{\partial t} \right)$$

The constant permeability can come out of the curl, and we can focus on the left side by applying Equation 2.8 and Equation 2.9:

$$\begin{aligned}
\nabla \times (\nabla \times \mathbf{E}) &= -\mu_0 \left(\nabla \times \frac{\partial \mathbf{H}}{\partial t} \right) \\
\nabla(\nabla \cdot \mathbf{E}) - \nabla^2 \mathbf{E} &= -\mu_0 \left(\nabla \times \frac{\partial \mathbf{H}}{\partial t} \right) \\
\nabla(0) - \nabla^2 \mathbf{E} &= -\mu_0 \left(\nabla \times \frac{\partial \mathbf{H}}{\partial t} \right) \\
-\nabla^2 \mathbf{E} &= -\mu_0 \left(\nabla \times \frac{\partial \mathbf{H}}{\partial t} \right)
\end{aligned}$$

We should note that the application of Equation 2.9 in the second line above was trickier than the manipulations suggest. In a nonlinear medium, Equation 2.9 does not imply that

$\nabla \cdot \mathbf{E} = 0$; however, as has been noted by other authors, this is typically a good assumption due to the weak nature of nonlinearities [5].

We now turn our attention to the right hand side of the above equations. First, we note that the time derivative commutes with the curl. (The curl operator deals with spatial variables.) Equation 2.7 can now be applied to obtain a familiar equation:

$$\begin{aligned} -\nabla^2 \mathbf{E} &= -\mu_0 \frac{\partial}{\partial t} (\nabla \times \mathbf{H}) \\ -\nabla^2 \mathbf{E} &= -\mu_0 \frac{\partial}{\partial t} \left(\frac{\partial \mathbf{D}}{\partial t} \right) \\ -\nabla^2 \mathbf{E} &= -\mu_0 \frac{\partial^2 \mathbf{D}}{\partial t^2} \end{aligned}$$

We now use Equation 2.5 to find our missing term for nonlinear media:

$$\begin{aligned} -\nabla^2 \mathbf{E} &= -\epsilon^{(1)} \mu_0 \frac{\partial^2 \mathbf{E}}{\partial t^2} - \mu_0 \frac{\partial^2 \mathbf{P_{NL}}}{\partial t^2} \\ \nabla^2 \mathbf{E} - \epsilon^{(1)} \mu_0 \frac{\partial^2 \mathbf{E}}{\partial t^2} &= \mu_0 \frac{\partial^2 \mathbf{P_{NL}}}{\partial t^2} \end{aligned} \tag{2.11}$$

We have now derived a wave equation that accounts for the nonlinear polarization response of a material. From the equation, we see that the nonlinear polarization appears as a source on the right hand side. This source drives solutions to the our linear wave equation, appearing on the left.

In the following, we will primarily be concerned with second harmonic generation. For simplicity, we will ignore higher order terms, and we will focus on the electric field $\mathbf{E}_2$ produced from the second-order polarization induced by the incident electric field $\mathbf{E}_1$. The second-order nonlinear polarization can then be written: $\mathbf{P_{NL}} = \epsilon_0 \chi^{(2)} \mathbf{E}_1^2 = \mathbf{P}_2$, which leads to a wave equation:

$$\nabla^2 \mathbf{E}_2 - \epsilon_{(1)} \mu_0 \frac{\partial^2 \mathbf{E}_2}{\partial t^2} = \mu_0 \frac{\partial^2 \mathbf{P}_2}{\partial t^2} \tag{2.12}$$

In the following section we will explore solutions to this equation. In considering these solutions and the dynamic growth of nonlinearly generated optical waves, we will encounter an important phenomenon for this thesis: phasematching.

2.2 Quasi-Phasematching and RQPM

As has been mentioned, our Cr:ZnSe/S laser will produce a second harmonic via random quasi-phasematching in its polycrystalline gain element. In the preceding section, we described the mathematical origins of second harmonic generation, and in this section we will delve deeper into the dynamics of the SHG process. However, before proceeding further mathematically, we pause to take a quick look at the physics of this process. SHG (Figure 2-1a) is a parametric process, meaning that the generated second harmonic happens instantaneously when the driving field illuminates the nonlinear material. In a parametric process (Figure 2-1b), there is no energy exchange between the optical field and the quantum states of the material. Not every incident photon will undergo this parametric process; in fact, very few of them do. As we will see in this section, to get a significant conversion of incident photons to SHG photons, phasematching will be required. In this section, we will solve our wave equation from the preceding section and uncover phasematching. We will also discuss quasi-phasematching (QPM) and random quasi-phasematching (RQPM).

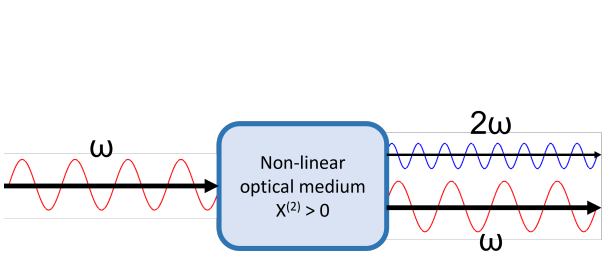

(a) Second Harmonic Generation

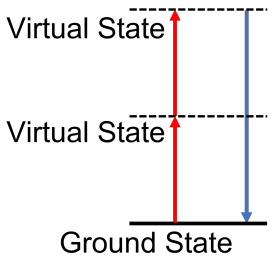

(b) Parametric Process

Figure 2-1: **Second harmonic processes:** (a) A wave of twice the fundamental frequency is produced when incident onto a non-linear media with a non-negligible $\chi^{(2)}$ parameter. (b) This generation is a parametric process in which the energy absorbed is spontaneously released and no energy is exchanged between the optical field and the medium.

2.2.1 Phasematching

In section 2.1, we found a wave equation the described the SHG process. This equation, dominated by the $\chi^{(2)}$ response, could be written:

$$\nabla^2 \mathbf{E}_2 - \epsilon_{(1)}\mu_0 \frac{\partial^2 \mathbf{E}_2}{\partial t^2} = \mu_0 \frac{\partial^2 \mathbf{P}_2}{\partial t^2} \tag{2.13}$$

Again, the above equation describes the generation of the second-harmonic electric field $\mathbf{E}_2$ produced from the second-order polarization induced by the incident electric field $\mathbf{E}_1$. The electric fields, $\mathbf{E}_1$ and $\mathbf{E}_2$ are assumed to take the form:

$$\mathbf{E}_i(t) = a_i(z) e^{j(k_i z - \omega_i t)} \tag{2.14}$$

Here, $a_i(z)$ is the slowly varying amplitude of the field, and the field is propagating in the z direction. The subscripts will represent the incident wave and the second harmonic (1 and 2 respectively), which also means $\omega_2 = 2\omega_1$. We have also introduced the wavenumber k_1, where $k_1 = n_1\omega_1/c$ and $n_1 = \left[\epsilon^{(1)}(\omega_1)\right]^{1/2}$. We can summarize these definitions:

$$\begin{aligned}
&i = 1 && \textit{(fundamental)} \\
&i = 2 && \textit{(SHG)} \\
&k_i = n_i\omega_i/c && \\
&n_i = \left[\epsilon^{(1)}(\omega_i)\right]^{1/2} && (\textit{Function of } \omega_i) \\
&c^2 = 1/\epsilon_0\mu_0 &&
\end{aligned}$$

Expanding the gradient term in Equation 2.13 and manipulating some parameters using the above definitions we find:

$$\left[\frac{\partial^2 a_2(z)}{\partial z^2} + 2jk_2\frac{\partial a_2(z)}{\partial z} - k_2^2 a_2(z)\right] e^{j(k_2 z - \omega_2 t)} - \epsilon^{(1)}\mu_0\frac{\partial^2 \mathbf{E}_2}{\partial t^2} = \mu_0\frac{\partial^2 \mathbf{P}_2}{\partial t^2}$$
$$\left[\frac{\partial^2 a_2(z)}{\partial z^2} + 2jk_2\frac{\partial a_2(z)}{\partial z} - k_2^2 a_2(z)\right] e^{j(k_2 z - \omega_2 t)} - \frac{n_2^2}{c^2}\frac{\partial^2 \mathbf{E}_2}{\partial t^2} = \frac{1}{\epsilon_0 c^2}\frac{\partial^2 \mathbf{P}_2}{\partial t^2}$$

Carrying out the time derivative on the left hand side,

$$\left[\frac{\partial^2 a_2(z)}{\partial z^2} + 2jk_2\frac{\partial a_2(z)}{\partial z} - k_2^2 a_2(z) + \frac{n_2^2 w_2^2}{c^2}a_2(z)\right] e^{j(k_2 z - \omega_2 t)} = \frac{1}{\epsilon_0 c^2}\frac{\partial^2 \mathbf{P}_2}{\partial t^2}$$

We can further simplify by noting $k_2 = n_2^2\omega_2^2/c^2$ and recalling from section 2.1 that $\mathbf{P}_2 = \epsilon_0\chi^{(2)}\mathbf{E}_1^2$:

$$\left[\frac{\partial^2 a_2(z)}{\partial z^2} + 2jk_2\frac{\partial a_2(z)}{\partial z} - k_2^2 a_2(z) + k_2^2 a_2(z)\right] e^{j(k_2 z - \omega_2 t)} = \frac{1}{\epsilon_0 c^2}\frac{\partial^2(\epsilon_0\chi^{(2)}\mathbf{E}_1^2)}{\partial t^2}$$
$$\left[\frac{\partial^2 a_2(z)}{\partial z^2} + 2jk_2\frac{\partial a_2(z)}{\partial z}\right] e^{j(k_2 z - \omega_2 t)} = \frac{1}{\epsilon_0 c^2}\frac{\partial^2(\epsilon_0\chi^{(2)}\mathbf{E}_1^2)}{\partial t^2}$$
$$\left[\frac{\partial^2 a_2(z)}{\partial z^2} + 2jk_2\frac{\partial a_2(z)}{\partial z}\right] e^{j(k_2 z - \omega_2 t)} = \left[-\frac{\omega_2^2}{c^2}\chi^{(2)}a_1(z)^2\right] e^{j(2k_1 z - \omega_2 t)}$$
$$\left[\frac{\partial^2 a_2(z)}{\partial z^2} + 2jk_2\frac{\partial a_2(z)}{\partial z}\right] e^{jk_2 z} = \left[-\frac{\omega_2^2}{c^2}\chi^{(2)}a_1(z)^2\right] e^{j2k_1 z}$$

From here, we apply the slowly varying amplitude approximation. This approximation amounts in saying that the second derivative with respect to z of the amplitude will be much smaller than k_2 times the first derivative. With this approximation, we find:

$$\left[2jk_2\frac{\partial a_2(z)}{\partial z}\right] e^{jk_2 z} = \left[-\frac{\omega_2^2}{c^2}\chi^{(2)}a_1(z)^2\right] e^{j2k_1 z}$$

In a final approximation, we say that, since the nonlinearity is weak, we will assume that

the incident wave amplitude remains approximately constant; so, $a_1(z) \approx a_1$. With this approximation, we introduce the phase-mismatch factor: $\Delta k = 2k_1 - k_2$, and we integrate over the length of the crystal (L):

$$2jk_2 \frac{\partial a_2(z)}{\partial z} = \left[-\frac{4\omega_1^2}{c^2} \chi^{(2)} a_1^2 \right] e^{j(\Delta k z)}$$

$$a_2(L) = \frac{\omega_1}{n_2 c} \chi^{(2)} a_1^2 \frac{e^{(j\Delta k L)} - 1}{\Delta k} \tag{2.15}$$

$$|a_2(L)|^2 \propto \text{sinc}^2(\Delta k L/2) \tag{2.16}$$

The important take away here is the dependence of a sinc squared function that determines the normalized intensity of the second harmonic as a function of the argument in Equation 2.16. A coherence length L_{coh} (Equation 2.17) can be defined as the distance at which the SHG wave becomes substantially out of phase with the incident wave. This definition can be visualized from the sinc squared function in Figure 2-2. When $L_{\text{coh}} \ll \frac{2}{\Delta k}$, the field amplitude grows quadratically with distance. At a coherence length of 1, $\text{sinc}^2(1) \approx 0.71$.

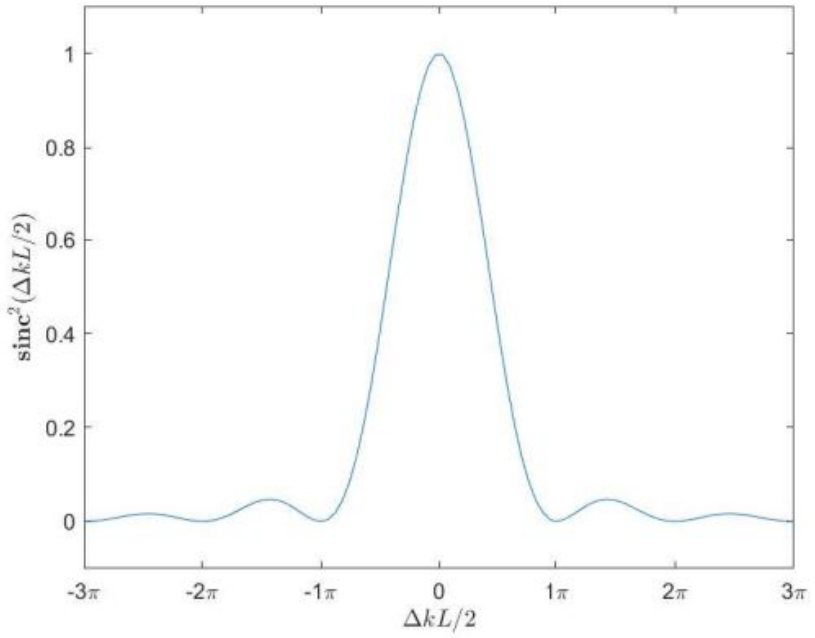

Figure 2-2: **SHG intensity vs wavevector mismatch** - The Intensity of the SHG can be normalized to show how the sinc square function limits the Intensity as a function of the phase mismatch factor.

$$L_{\text{coh}} = \frac{2}{\Delta k} \tag{2.17}$$

From the above analysis, we see that SHG is optimally generated when $\Delta k = 0$, that is, when our waves are perfectly phasematched. Perfect phasematching amounts in $k_2 = 2k_1$ (for SHG). However, in real materials, dispersion causes the wavenumber of k_2 to be slightly different than that of $2k_1$ (Figure 2-3).

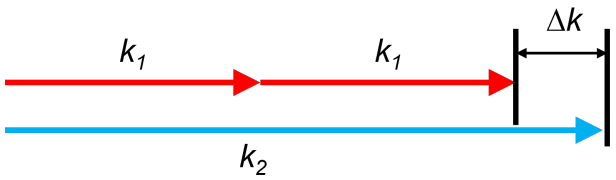

Figure 2-3: **Phase mismatch factor** - At first, it would seem that two collinear beams should exhibit a wavevector mismatch of zero due to the parametric process. However, other effects, such as dispersion, can also alter the wavevector which will make $\Delta k \neq 0$

A common method for overcoming dispersion and achieving perfect phasematching involves exploiting birefringence. In a birefringent crystal, the refractive index depends on the polarization direction. Using such crystals positioned at specific angles, perfect phasematching can be achieved. However, this technique can be challenging and requires specific birefringent properties. There is another technique for achieving phasematching, without birefringence: quasi-phasematching (QPM).

2.2.2 QPM and RQPM

Quasi-phasematching achieves phasematching by dividing the nonlinear medium into many small, alternating domains. First there will be a domain with significant $\chi^{(2)}$ but with no phasematching. After around a coherence length, this domain will terminate. The next domain will not have a significant $\chi^{(2)}$, and the waves will propagate freely. After a certain distance, the waves will return to being in phase, and another domain with significant $\chi^{(2)}$ will be placed. Mathematically, these alternating domains can interpreted as periodically introducing a $(-1)^n$ factor into Equation 2.15. This new equation can then be integrated over the domain spacing, Δ, and as the sum of the the number of domains:

$$a_2(L) \propto \sum_{n=0}^{N-1} (-1)^n \int_{\Delta n}^{\Delta(n+1)} e^{j\Delta kz}$$

The "periodically poled" nonlinear crystal has its properties alternated at a periodicity of less than or equal to twice the coherence length L_{coh} from Equation 2.17. Although QPM is not as efficient as perfect phase-matching, its efficiency can still be significant enough to allow the second harmonic to grow as seen in Figure 2-4.

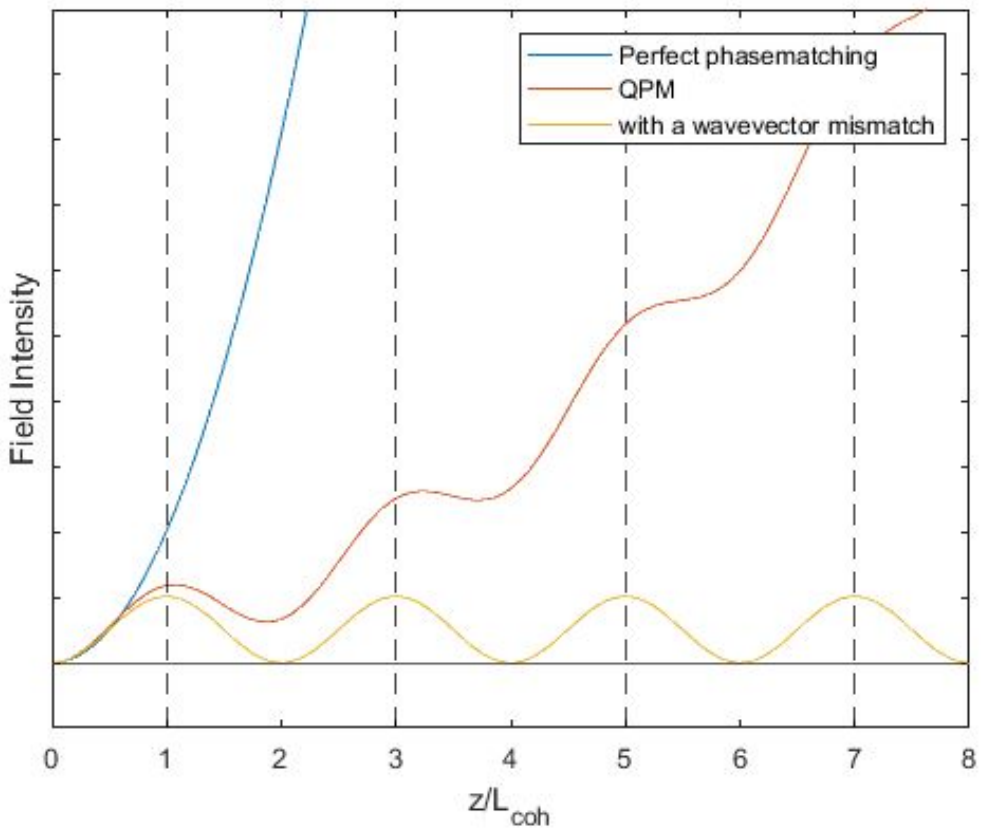

Figure 2-4: **SHG field intensity due to quasi-phasematching** - The field intensity of the second harmonic is plotted as a function of normalized coherence length. The blue trace can be achieved using birefringence, while the yellow trace shows the square since function limitation when a substantial mismatch is experienced by the second harmonic. When quasi-phasematching is engineered, the length of one domain can be seen by the vertical dashed lines equalling 2 coherent lengths. Although QPM is nowhere near as efficient as perfect phasematching, a second harmonic can grow to a point where it can become useful.

Our laser system is based on a Cr-doped ZnSe/S crystal. The ZnSe/S is actually a polycrystalline material, and this material exhibits an interesting phenomenon called random

quasi-phasematching (RQPM). The randomness in the QPM comes from the structure of this nonlinear crystal; the crystal is composed of a group of randomly oriented single crystal grains that are individually around tens of microns in size [3]. For the case of QPM, the crystals are periodically reversed in orientation. This is not the case for Cr:ZnS as the single crystals are randomly oriented. However, the grain size is just about the right size, relative to the coherence length, to enable second harmonic generation of $\sim$2 μm light. The RQPM process does not reach the efficiency of a QPM process, and consequently, the SHG generation lies far below the efficiency of perfect phasematching. Nonetheless, the second harmonic produced in our system is far from negligible; the SHG output power is >200 mW, and it could be of use for applications.

2.3 Autocorrelation

In the final section of this chapter, we will overview the basics of ultrafast laser pulse measurement. First, we will consider the essentials of ultrafast laser pulses; next, we will describe fundamental techniques for measuring these parameters.

When a laser pulse is characterized, it means that certain parameters of the pulse are known. Take this arbitrary pulse:

$$e(t) = a(t) \exp(j\omega_0 t) \tag{2.18}$$

Here, $a(t)$ is the pulse envelope. In general this envelope is complex, and contains phase variations in both time and frequency domains:

$$a(t) = |a(t)| \exp(j\phi(t)) \tag{2.19}$$

$$A(\omega) = |A(\omega)| \exp(j\Psi(\omega)) \tag{2.20}$$

When a pulse is fully characterized, it means that all parts of Equation 2.18 are known. A pulse's carrier frequency is determined by ω_0. The pulse duration is determined by the

envelope function as well as the temporal and spectral phases. Knowing these and other aspects of the pulse allows for tailoring the pulse to the needs of applications.

Pulse characterization is no small task. After all, how do you measure an event so fast, that the event itself is the fastest thing you can produce? What do you measure it with? Typically, fast photodiodes and oscilloscope can be made with a response time of hundreds of picoseconds; however, even this impressive speed is very slow compared to a femtosecond laser pulse.

As a comparison, imagine a person experimentally measuring how long it takes for a fired bullet to traverses a distance of 20 meters using a stopwatch. A standard military-issued M16 5.56-millimeter rifle has a muzzle velocity of around 950 meters per second. If we would like to know how long it takes for the bullet to traverse 20 meters, then we simply divide the distance by its velocity to obtain the elapsed time. Using these values, we will find out that the bullet traveled for roughly 21 milliseconds until it crossed the 20-meter mark. Let us say that we did not know the muzzle velocity of this rifle. If a stopwatch is to be used, the average human reaction time to sound is around 150 milliseconds (the time it would take you to start the stopwatch after hearing the rifle go off). The average human reaction time to sight is around 250 milliseconds (the time it would take to stop the stopwatch after seeing it pass the 20-meter line). Of course, brain registration can happen much faster, but the time it takes to process the information and create a response for the body to follow adds to the total reaction time. Nevertheless, you would fail to even start the stopwatch before the bullet reaches the 20 meters. This is because the event that you are trying to measure is faster than your measuring device.

This question of how we will measure a pulse so fast that it is the fastest thing that we can make has a simple answer: we will use the pulse to measure itself. In its simplest form, this technique is called autocorrelation. The first autocorrelation that will be discussed is the field autocorrelation, which uses simple linear measurement techniques to obtain information about a laser pulse, but not all.

2.3.1 Field Autocorrelation

The essential experimental setup for the field autocorrelation is the Michelson interferometer, as shown in Figure 2-5. From here, we can use our arbitrary pulse from Equation 2.18 as our input electric field. After the pulse passes the beamsplitter, two identical pulses will travel different distances: l_1 and l_2. These lengths are traveled twice by the individual pulses and are recombined at the beamsplitter with one arriving later than the other. These lengths are related to a time delay by $t_1 = 2l_1/c$ and $t_2 = 2l_2/c$, where c is the speed of light.

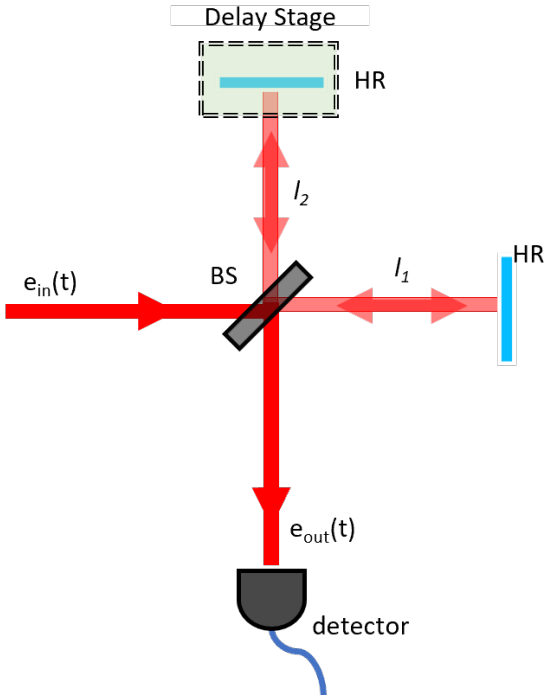

Figure 2-5: **Field autocorrelator setup** - BS: Beamspliterr, l:length. Top view of a field autocorrelator that also resembles a Michelson Interferometer.

A 50-50 beamsplitter will separate the pulse yielding two pulses of equal power and half the power of the original pulse. This equates to multiplying the input pulse field by a factor of $1/\sqrt{2}$ each time the pulse passes through the beamsplitter. In the Michelson interferometer, the pulse would pass through the beamsplitter two times before reaching the photodetector. This results in two identical pulses delayed in time at half the value as the input field:

$$e_{\text{out}}(t) = \frac{1}{2}\text{Re}\left\{E(t-t_1) + E(t-t_2)\right\} \tag{2.21}$$

The output power will then be,

$$\begin{aligned}
P_{\text{out}}(t) &= \frac{1}{4}\left|E(t-t_1) + E(t-t_2)\right|^2 \\
P_{\text{out}}(t) &= \frac{1}{4}[E(t-t_1) + E(t-t_2)][E^*(t-t_1) + E^*(t-t_2)] \\
P_{\text{out}}(t) &= \frac{1}{4}[|E(t-t_1)|^2 + |E(t-t_2)|^2 + 2\text{Re}\{E(t-t_1)E^*(t-t_2) + \text{c.c.}\}]
\end{aligned}$$

The photodetector will be slow compared to the combined pulse and the time delays, so the time-integrated intensity will consequently be measured. We can also change our reference frame so that the time-integrated intensity is independent of the average pulse delay, and the integral of the cross terms depends only on the relative delay (τ) between the two pulses ($\tau = t_2 - t_1$):

$$\begin{aligned}
\int dt P_{\text{out}}(t) &\propto \int |E(t)|^2 + |E(t-\tau)|^2 + 2\text{Re}\{E(t)E^*(t-\tau)\}dt \\
&\propto \underbrace{2\int |E(t)|^2 dt}_{\text{Pulse Energy}} + 2\text{Re}\underbrace{\int E(t)E^*(t-\tau)dt}_{\text{Field autocorrelation}}
\end{aligned}$$

$$G_1(\tau) = \int E(t)E^*(t-\tau)dt \tag{2.22}$$

Now that we have an equation for our field autocorrelator, let us use MATLAB to see what information can be extracted from this equation. We begin again by using Equation 2.18 as our pulse and choosing an arbitrary envelope, for instance a parabolic pulse shape (Equation 2.23). (Note: in our equation for the parabolic pulse, the pulse field should be zero for $|t| > \tau_d$.) Choosing a pulse duration of $\tau_d = 10$ fs and a carrier wavelength of $\lambda_0 = 800$ nm, the resulting pulse will appear as in Figure 2-6a. Figure 2-6b is the resulting

field autocorrelation (FAC) as calculated by Equation 2.22.

$$E(t) = \left(1 - \frac{t^2}{\tau_d^2}\right) \exp\left(j\omega_0 t\right) \tag{2.23}$$

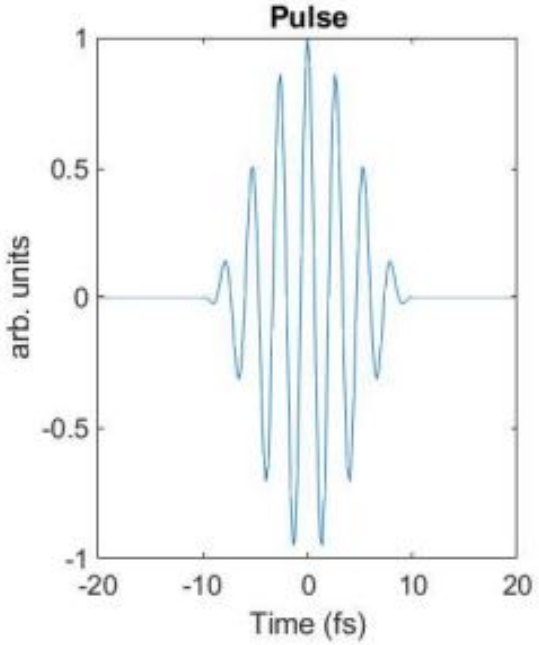

(a) A parabolic pulse with a pulse duration of $\tau_d = 10$ fs

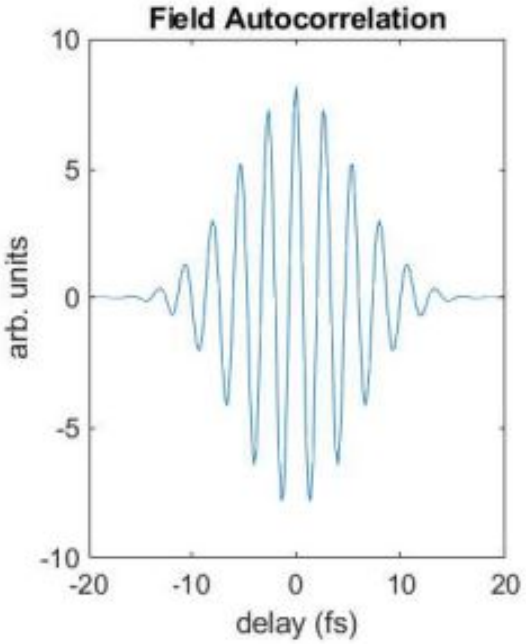

(b) FAC simulation result from the Parabolic pulse showing a correlation time: τ_c

Figure 2-6: **Parabolic pulse and its FAC** - (a) Equation 2.23 is plotted here for side-by-side comparison with its FAC measurement (b)

A question to ask now would be: Could we somehow obtain the pulse duration (τ_d) from the correlation time (τ_c)? One might be tempted to think so, but the answer is no. Plotting both the Fourier transform of $G_1(\tau) \longrightarrow G(\Omega)$ and the power spectrum of $E(t) \longrightarrow |\tilde{E}(\omega)|^2$ will show that the field autocorrelation and the spectrum of $E(t)$ are identical (Figure 2-7).

What does this tell us? The correlation time is approximately the inverse of the optical bandwidth ($\tau_c \approx 1/\Delta\omega$). When the power spectrum of $E(t)$ is measured or calculated, which consequently takes the modulus square of Equation 2.20, the spectral phase information is lost. We should note that although the field autocorrelation is not useful for pulse duration measurement, it is extremely useful for pulse spectrum measurements. The field autocorrelation forms the foundation of an extremely successful spectral measurement technique called Fourier Transform Infrared Spectroscopy (FTIR).

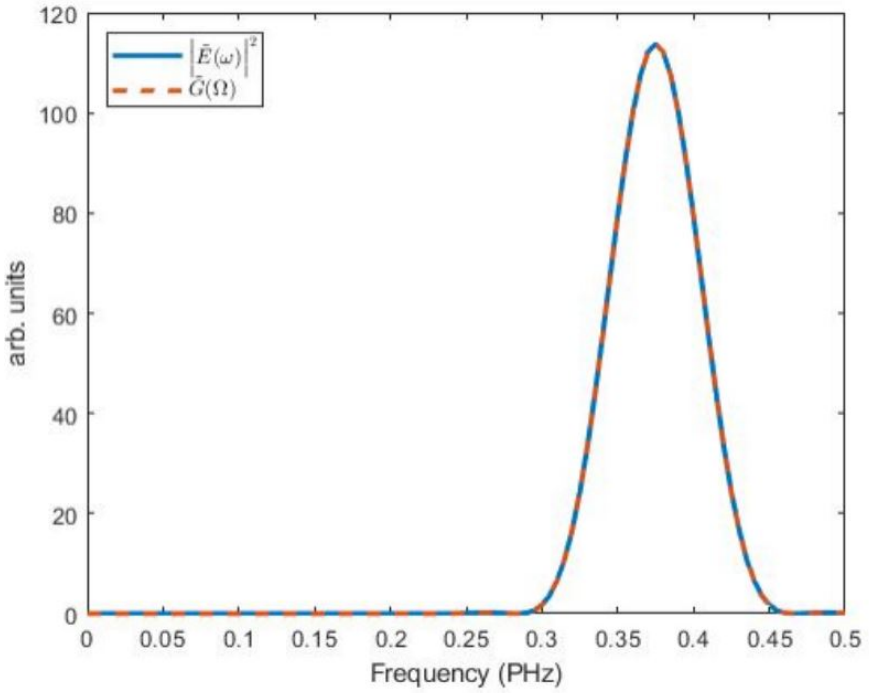

Figure 2-7: **Power spectra and FAC comparison** - The Fourier Transform of the field autocorrelation is plotted on the same axis as the spectra of the electric field. Both of these traces are identical which results in important implications concerning the Field Autocorrrelator.

2.3.2 Intensity Autocorrelation

We have seen that the field autocorrelation does not give us any information about the pulse beyond the power spectrum. By adding a nonlinear $\chi^{(2)}$ crystal into the experimental setup, as shown in Figure 2-8, a second harmonic of the incident light is generated. This generated second harmonic will be able to tell us about our incident pulses in the time domain, and this non-collinear setup is referred to as the intensity autocorrelation (Intensity AC).

In the intensity autocorrelator shown in Figure 2-8, the iris eliminates the input pulses including second harmonics created by the individual input beams. What we are left with is the time average intensity of the interference-generated second harmonic as a function of delay time.

$$G_2(\tau) = c_2 \int I(t)I(t-\tau)dt \tag{2.24}$$

Here, $I(t) \propto |E(t)|^2$ and c_2 is a normalized constant. Let us now consider two Gaussian-

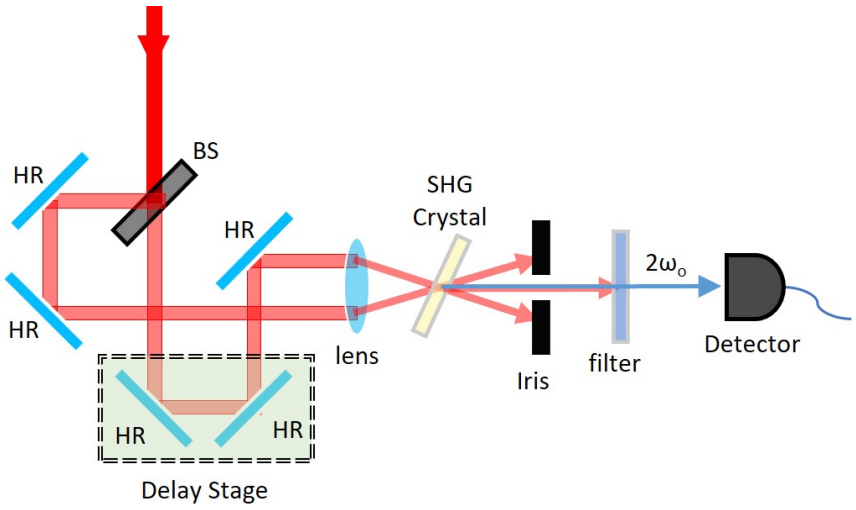

Figure 2-8: **Intensity autocorrelation setup** - The intensity autocorrelator has the beams traveling coplanarly but not collinearly. This prevents the SHG produced by the individual beams from traveling toward the detector. For this reason, this technique is also named the *Background-free Autocorrelation*.

shaped laser pulses:

$$E(t) = \exp\left(-\frac{t^2}{2\tau^2}\right)e^{j\omega_0 t} \tag{2.25}$$

Pulse 1 has a central wavelength of 800 nm and Pulse 2 has a central wavelength of 1273 nm. Both pulses will have a pulse width of 10 fs and will travel 5 mm through fused silica before reaching the nonlinear crystal. In fused silica, it is expected that the 800 nm pulse will broaden and the 1273 nm pulse will remain roughly the same in terms of its width. It is also expected that the 1273 nm pulse will exhibit some characteristics associated with higher-order dispersion.

As seen in Figure 2-9, it is apparent that a sense of the pulse's duration can be observed due to the clear indication of the pulse broadening. However, the higher-order dispersion details that Pulse 2 should exhibit are lost.

2.3.3 Interferometric Autocorrelation

The Intensity AC measurement can be modified in an interesting way by setting the experiment as in Figure 2-10. In this configuration, the second harmonic light created by the

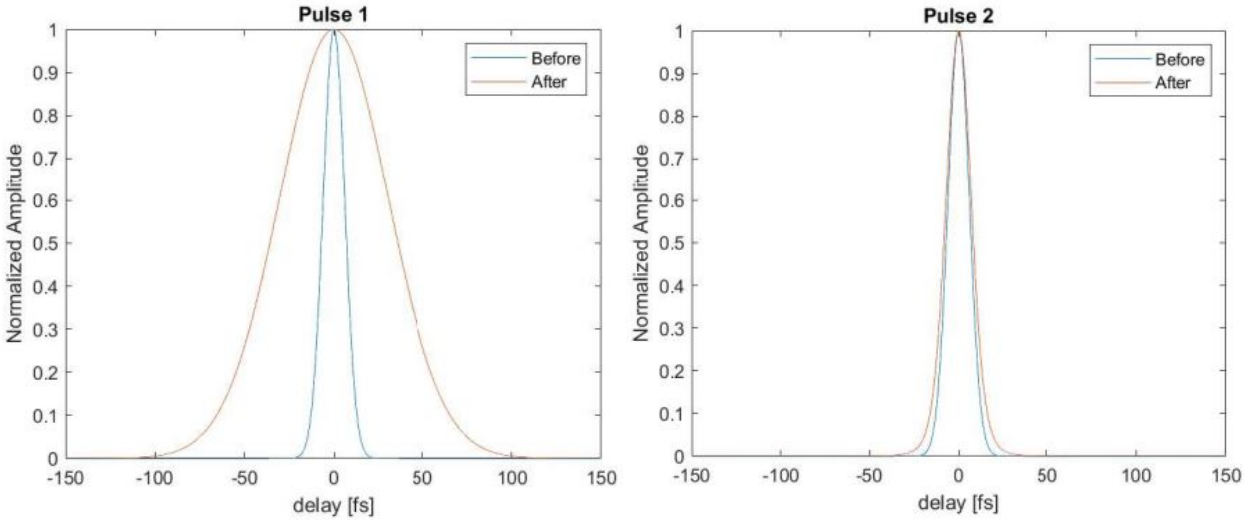

(a) (b)

Figure 2-9: **Intensity AC example** - (a) The intensity AC of the first pulse shows some broadening after fused silica was placed in its path (as expected) showing that the intensity AC can give some information about the pulse duration of the pulse. (b) shows the second pulse experiencing no pulse duration which is also expected from a 1273 nm central wavelength but has no characteristics indicating the known higher-order dispersion traits.

interaction of the two beams combines coherently with the second harmonics created by the individual beams. This collinear setup is the interferometric autocorrelation, which is also called the fringe-resolved autocorrelation (FRAC), so as to not be confused with the abbreviation of the previous setup.

The pulse at the output of the interferometer, which will then be incident to the SHG crystal, is the same as our field autocorrelator Equation 2.22. The field then goes through the SHG crystal and outputs a field which is proportional to the square of the input field. The photodiode at the output now measures the time-integrated second-harmonic power to obtain:

$$G_3(\tau) = c_3 \int |E(t) + E(t-\tau)|^4 dt \tag{2.26}$$

Here, the c_3 is a normalized constant such that $G_3(-\infty)$ is equal to one. This will normalize the trace with the background, which provides a rough sanity check.

Carrying out the algebra one will find four main terms that describe the interactions happening inside the crystal, including a very familiar term.

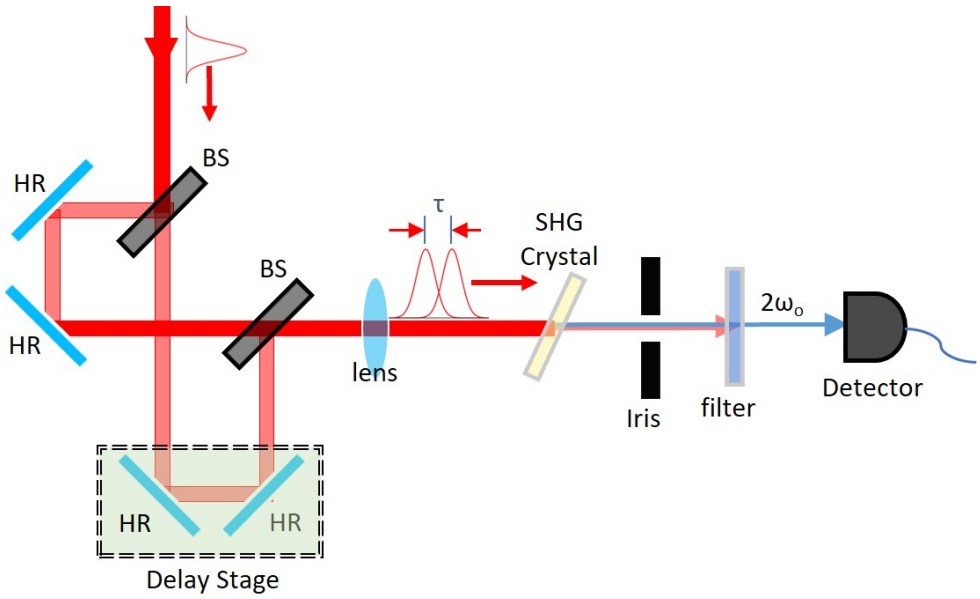

Figure 2-10: **Interferometric autocorrelator** - Collinear beams are allowed to interfere within the SHG crystal as a function of delay time. A filter is then added at the end two measure the second harmonic interferogram produced by the collinear beams.

$$
\begin{aligned}
G_3(\tau) &= \int I(t)^2 + I(t-\tau)^2 dt && \text{Constant} \\
&+ 2\int I(t)I(t-\tau)dt && \text{Intensity Autocorrelation} \\
&+ \int \left[I(t) + I(t-\tau)\right] E(t)E^*(t-\tau)dt + c.c && \text{Modified Interferogram of E(t)} \\
&+ \int E(t)^2 E^*(t-\tau)^2 dt + c.c && \text{Interferogram of Second Harmonic}
\end{aligned}
$$

The constant term is useful in verifying the validity of our measurement. In a FRAC trace, the peak-to-background ratio should be 8:1 [6], which is a good sanity check and a good indication that there is proper alignment. (This is because, at $\tau = 0$, all the integrals become identical.)

$$
\begin{aligned}
G_3(0) &= \int I(t)^2 + I(t)^2 dt \\
&+ 2\int I(t)I(t)dt \\
&+ \int \left[I(t) + I(t)\right] I(t)dt \\
&+ 2\int I(t)^2 dt
\end{aligned}
$$

Therefore,

$$
\begin{aligned}
G_3(\tau)|_{\max} = G_3(0) &= 8 \\
G_3(\tau \longrightarrow \pm\infty) &= 1 \\
G_3(\tau)|_{\min} &= 0
\end{aligned}
$$

The second term is the intensity autocorrelation which we have seen before. The third and fourth terms are the inteferograms that occur in ω and its second harmonic 2ω, which will yield fringes with respect to the delay.

Let us see what information can be made visible using the same two Gaussian pulses from the previous section. As a reminder, the "Before" trace demonstrates the FRAC before placing fused silica in the path of the laser pulse.

The broad pedestal on which the 'After' trace in Figure 2-11a sits contains information about the broadened pulse. Additionally, how some fringes have been embedded into the wings is a clear indication that the pulse is chirped. Figure 2-11b also demonstrates that a longer pulse duration will correspond to a longer correlation time, and, most importantly, the higher-order dispersion that should be expected from Pulse 2 is more visible in the ripples extending at the wings of the "After" trace in comparison with no ripples from the "Before" trace.

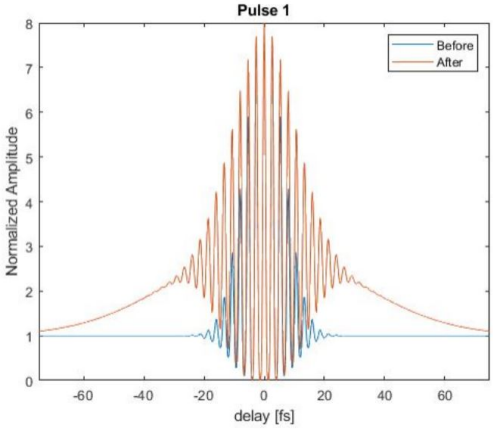

(a) Pulse 1 FRAC

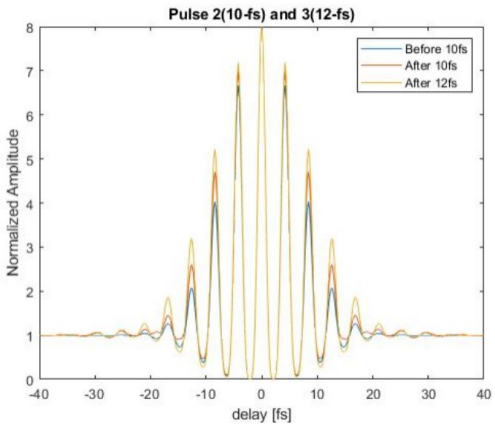

(b) Pulse 2 FRAC

Figure 2-11: **FRAC example** - (a)Pulse 1's FRAC simulation results show that the pulse has been broadened and chirped indicated by the pedestal it sits on and the extended fringes at the wings. (b) Pulse 2's FRAC simulation results show signs of higher-order dispersion terms indicated by the ripples that spread out at the wings.

Chapter 3

Transimpedance Amplifier Design and Testing

In this thesis we aim to characterize the second harmonic generation from a ZnSe/S crystal when driven by femtosecond-duration, $\sim$2 μm mid-infrared laser pulses. As described in the preceding chapters, our characterization will rely on nonlinear autocorrelations. The nonlinearity in these autocorrelations will inevitably lead to a weak signal. Specifically, as we will describe in the following chapter, our autocorrelator will rely on second harmonic generation in a thin birefringent crystal. The second-harmonic generation signal coming from this thin crystal will be extremely weak. This weak optical signal will be converted to an electrical signal on a silicon photodiode.

The weak optical signal will lead to a weak electrical signal, and in order to retrieve autocorrelation measurements with high signal-to-noise ratio (SNR), we will need to amplify this electrical signal. As we will describe in this chapter, our silicon photodiode can be modeled as a current source with a shunt resistance and capacitance. The current output from the current source is proportional to the optical power incident on the photodiode. Therefore, to amplify our electrical signal, we require a current amplifier, or a *transimpedance amplifer* (TIA). In this chapter, we will describe the design and testing of a high-gain and low-noise TIA for the effective retrieval of weak optical signals on a large-area silicon photodiode.

This chapter is organized as follows. First, we will provide background information on photodiodes; specifically, we will describe an electrical model for the photodiode used in this

work. Next, using this electrical model, we will describe the design of a high-gain, low-noise TIA; the analysis of noise in this TIA will be a priority of this section. Lastly, we will describe the construction of our TIA for our autocorrelator and the testing and performance of this amplifier.

3.1 Photodiode Basics

A photodiode is a semiconductor device, typically composed of a singular *pn* junction. The region where these *p*- and *n*-layers meet is the depletion region, and it is where a built-in voltage develops and creates an electric field that points from the *n*-layer to the *p*-layer. When a photon strikes the *p*-layer or the *n*-layer, the created electron-hole pair quickly recombines back into the material. However, when a photon strikes the depletion layer, the induced electric field in that region allows the electron-hole pair to split and form a current (Figure 3-1a)[7].

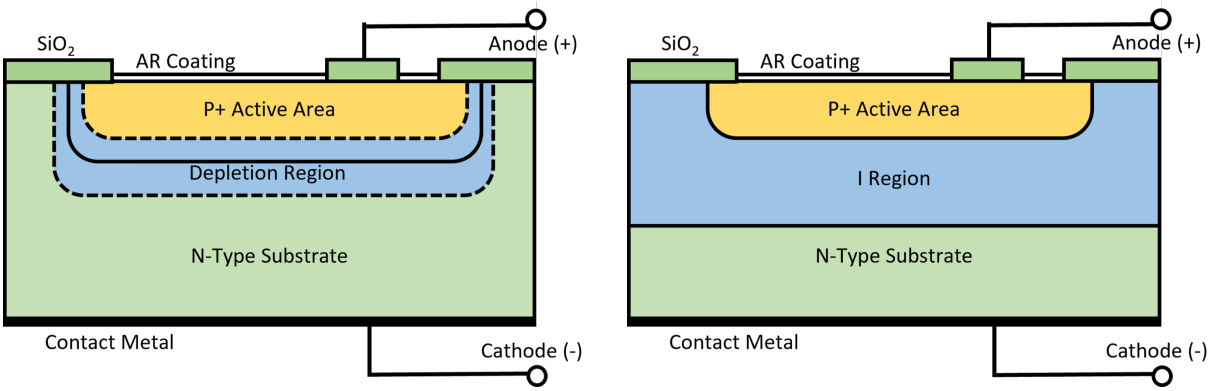

(a) P-N Cross-section (b) PIN Cross-section

Figure 3-1: **Photodiode cross-sections:** (a) The cross section to a P-N photodiode is similar to that of a diode, only a photodiode has an exposed active area with anti-reflective coating to allow the absorption of light. (b) For a PIN photodiode, an intrinsic region is inserted between the *p*-layer and the *n*-layer and acts like a depletion region itself.

The photodiode used in this thesis is the S1223-01 from Hamamatsu Photonics, and this type of photodiode is a PIN-photodiode. Unlike the *pn*-photodiode, the PIN-photodiode has an extra intrinsic layer in between the *p*-layer and the *n*-layer (Figure 3-1b). The benefits of having an intrinsic layer sandwiched in between the *pn* junction increases the depletion

region length which allows more photons to reach the depletion region, thus increasing the overall sensitivity of the device. Furthermore, the device's junction capacitance will decrease making it capable of handling faster changes in intensity.

Mode of Operation

A photodiode is typically operated in one of two modes: unbiased or reverse biased. The unbiased mode, also referred to as the photovoltaic mode, is a common mode used when measuring low light intensities. This is because in this mode the photodiode produces the minimal amount of dark current when no bias voltage is applied. This can be visualized by the I-V graph [8] of a diode in Figure 3-2. At V=0, the photodiode produces virtually no dark current, a key point when dealing with low signals and minimizing noise.

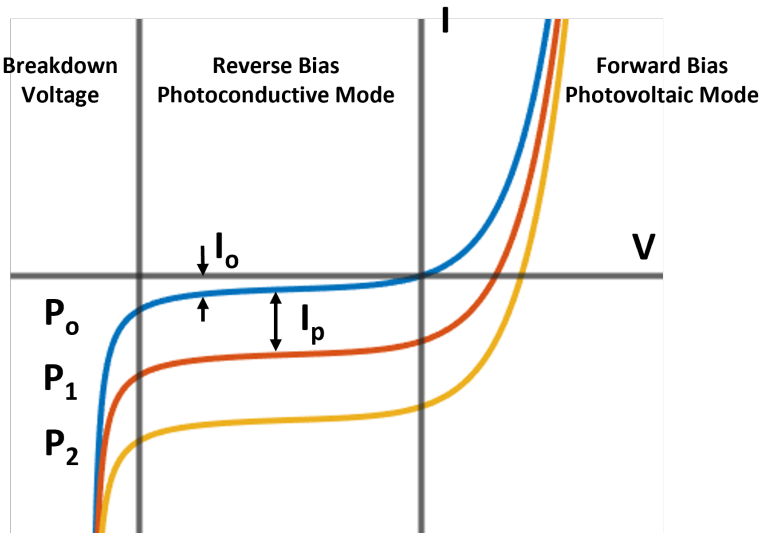

Figure 3-2: **Photodiode I-V** - The I-V characteristics of a photodiode is exactly like a pn junction diode, with an added vertical shift that is dependent on the incident light.

In the case of the reverse biased mode (photoconductive), a positive potential is placed on the cathode (n-layer) and a negative potential is placed on the anode (p-layer). Doing so increases the depletion layer, thus allowing a larger area to absorb photons. As before, this also means the junction's capacitance is decreased, further improving the device's response time. However, unfortunately, reverse biasing a photodiode allows for more dark current to infect the signal. Since the experimental setup created in this thesis favors low noise as

opposed to a higher response time, a PIN photodiode is preferred.

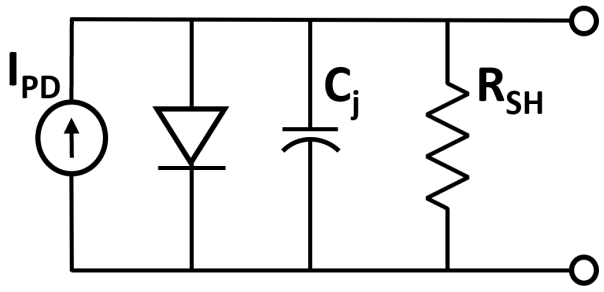

Figure 3-3: **Photodiode model** - Typical model used when performing circuit analysis on a photodiode.

In Figure 3-3, we show circuit model for a photodiode. The junction Capacitance (C_j) is typically found in the component's datasheet (20 pF for our photodiode)[9], while the shunt resistance can be found experimentally by applying a small voltage (around -10 mV to -5 mV) and recording its dark current. Typically, R_{sh} is on the order of 100MΩ to 1000s of MΩ.

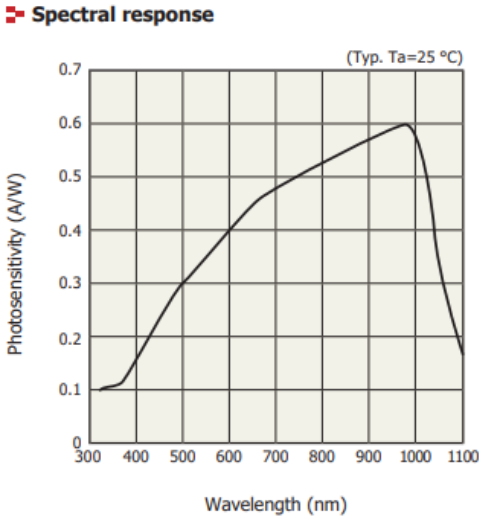

Figure 3-4: **Photosensitivity** - S1223-01

In Figure 3-4, we show the photosensitivity of our photodiode. The SHG produced in our experiments is expected to have a power of around 1 nW. This corresponds to a generated current of 300-400 pA assuming the wavelength of the SHG will span 500-600 nm. A low-noise TIA capable of handling such small currents, while keeping signal integrity, will

be required.

3.2 TIA Design

As discussed at the beginning of this chapter, we expect that the nonlinear light, that is, the second harmonic generation (SHG), in our autocorrelator will be very weak. Let us assume that this SHG will have a power of ∼1 nW. The SHG will span ∼500-600 nm in wavelength (that is, double the frequency of our input, ∼1-1.2-μm, pulses). So, based on the data from the preceding section, we expect that our photodiode will generate ∼300-400 pA of current. To bring these small currents to reasonable levels for measurement, we will target an amplifier with a gain of $10^6 - 10^8$ V/A (Ω). Furthermore, for sufficient SNR, we will aim for our amplifier to have input noise spectral density of ∼1 pA/$\sqrt{\text{Hz}}$ or below.

In the following section, we will describe our design and design procedure to meet these requirements. Firstly, we will focus on noise. We will describe the overall design or our amplifier and our noise model for the amplifier, and we will describe how we estimate output noise due to the voltage and current noise characteristics of our amplifier components. Next, we will overview our simulations of amplifier performance and describe how these guided our design. Lastly, we will present an initial design for construction and testing.

3.2.1 Overall Design and Noise Model

The overall design of our TIA is illustrated in Figure 3-5. In this figure, the photodiode circuit model is identified in the dash-dotted box. Quick inspection of the amplifier design reveals that our TIA closely resembles a conventional, operational-amplifier-based (op-amp-based) inverting amplifier. The only difference is that our TIA has a current source, instead of a voltage source, input (and, accordingly, the input resistor in the non-inverting amplifier design has been removed). This design is the standard TIA design; in the circuit, the full current of the photodiode should flow trough the feedback impedance, $R_2||C_2$ (assuming an ideal op amp), and the gain of the TIA should therefore be approximately equal to the feedback resistance. Additionally, to ensure this simple, ideal-like behavior, it is critical that the op amp has very low input bias current. (Again, for our design, we want nearly all of

the photodiode current to flow through the feedback resistor.) Therefore, in our TIA design it is necessary to have FET-input op amps, as their input currents are extremely low.

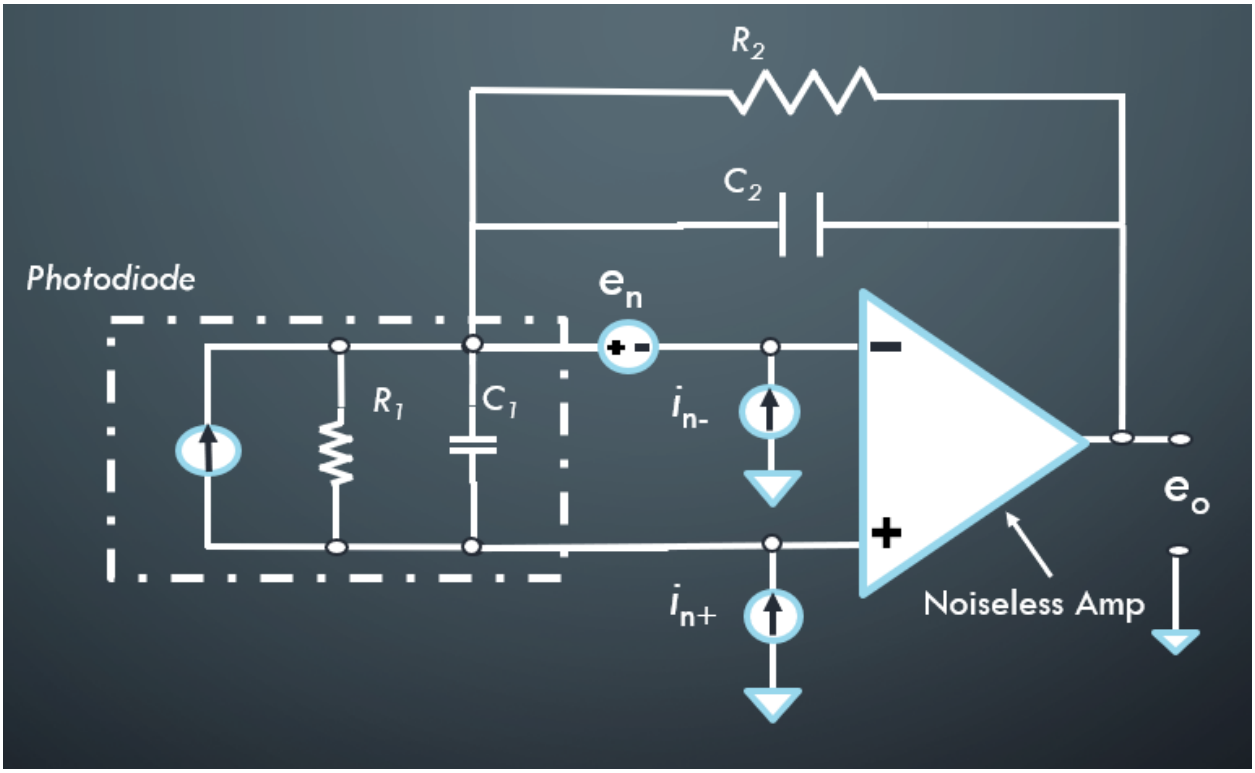

Figure 3-5: **TIA: Overall Design and Noise Model**. The overall design resembles the conventional inverting amplifier with a current input and the input resistance removed. The photodiode circuit model is shown in the dash-dotted box. The voltage noise contribution is modeled by a frequency dependent voltage source (e_n) that will be amplified by the circuit. The current noise contribution is modeled by frequency dependent current sources (i_{n-} and i_{n+}).

Noise comes from a variety of electrical and physical phenomena that stem from our op amp and from the passive components that make up the feedback network in our TIA. These noise sources include shot noise, thermal noise, and flicker noise. Shot noise is frequency independent and an inherent property of discretized currents; thermal noise is similarly frequency independent and stems from fluctuations associated with thermal motion of carriers; and flicker noise falls off as one over frequency and arises from a variety of physical processes in different devices.

For our analysis, we will model the noise in our TIA as being due primarily to technical noise in the op amp and due to thermal noise in the feedback resistor. The technical noise in

the TIA is broken into two components: voltage noise and current noise. Figure 3-5 shows a basic noise model that will allow us to account for technical noise in the TIA. Specifically, we will model the voltage noise as a voltage source, e_n, in series with the inverting input of an noiseless op amp, and we will model the current noise as current sources, i_{n-} and i_{n+}, connected to the input terminals of a noiseless op amp. This circuit model will allow us to determine how noise sources affect the overall output noise of our amplifier. (We should note that the values and behaviors of these technical noise sources, including e_n, i_{n-}, and i_{n+}, are provided in datasheets for low-noise op amps.)

3.2.2 Voltage Noise

With the noise model shown in Figure 3-5, we are now ready to analyze the impact of technical, op-amp noise on the output of our TIA. (The analysis in the following section closely parallels that from Ref. [10].) We will analyze the voltage and current noise independently and combine them via superposition. In this section, we will consider voltage noise.

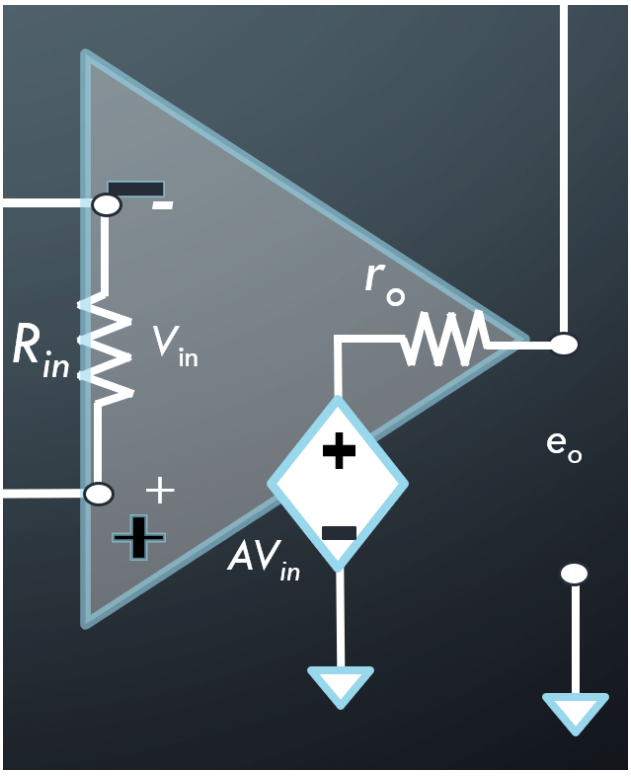

Figure 3-6: **Opamp Model** - Rin and Ro at the opamp

For the voltage noise analysis, we will we assume the ideal opamp case, as shown in Figure 3-6, so that r_0 is small and R_{in} is large. The photodiode will remain unbiased. This will decrease the response speed of the photodiode (higher photodiode capacitance, C_1), but it will also decrease the dark current that it produces. This trade-off will work in our favor since we do not need the response speed to be fast, as will be described in chapter 4. (We should note: the unbiased photodiode means that our non-inverting input will be grounded and one of the current noise contributions can be ignored.) Furthermore, in the voltage noise analysis, the current sources can be replaced by open wires and our passive components can be combined into equivalent impedances.

In Figure 3-7a, we show the equivalent circuit for the analysis of the voltage noise. Again, current sources have been zeroed (replaced by open wires), and our passive components have been lumped into equivalent impedances. Specifically Z_1 and Z_2 are the equivalent impedance of a resistor and capacitor in parallel. Z_1 represents the parallel combination of R_1 and C_1; $Z_1 = R_1||C_1 = \left(\frac{1}{R_1} + \frac{j\omega C_1}{1}\right)^{-1} = \frac{R_1}{1+j\omega R_1 C_1}$. Z_2 represents the parallel combination of R_2 and C_2; $Z_2 = \frac{R_2}{1+j\omega R_2 C_2}$. Lastly, note that we have replaced the noiseless op amp with a voltage-dependent voltage source. The output voltage, e_0, is equal to the open-loop gain of the noiseless op amp, $A(\omega)$, multiplied by the input voltage at the input of the noiseless op amp, V_{in}.

Rearranging the circuit in Figure 3-7a, we find the circuit in Figure 3-7b. We see that our voltage noise can be calculated by a simple voltage divider analysis:

$$
\begin{aligned}
e_n - V_{\text{in}} &= e_0 \frac{Z_1}{Z_1 + Z_2} \\
e_n - \frac{e_0}{A} &= e_o \frac{Z_1}{Z_1 + Z_2} \\
e_n &= e_o \left(\frac{Z_1}{Z_1 + Z_2} + \frac{1}{A} \right)
\end{aligned}
$$

In the above, we use the fact that the output voltage is equal to the open-loop gain of the noiseless op amp multiplied by the input voltage, $e_0 = AV_{\text{in}}$. Now, defining the feedback

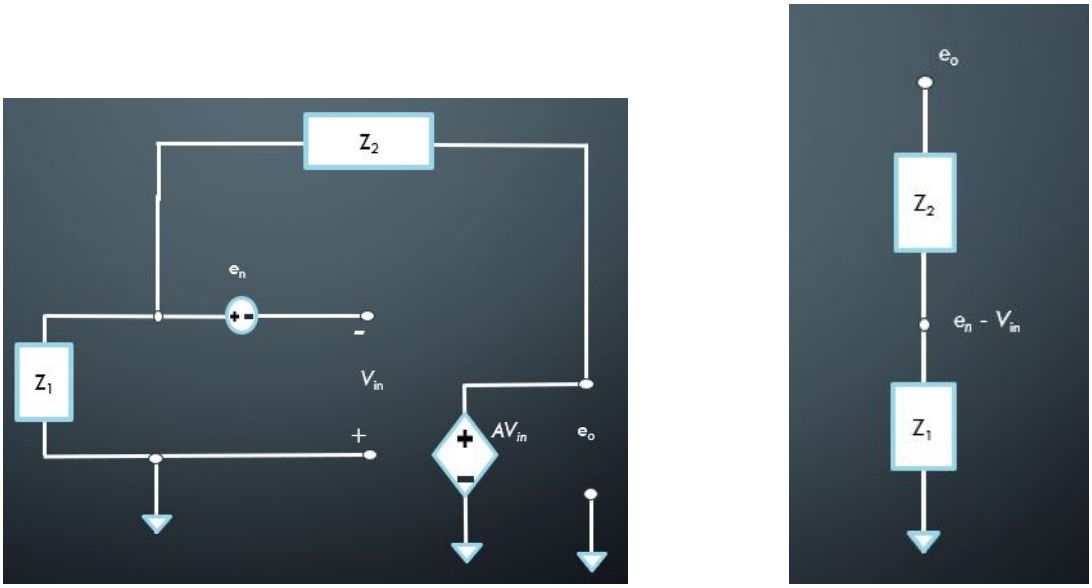

(a) Equivalent voltage noise contribution circuit (b) Rearrangement of the same circuit

Figure 3-7: **Voltage noise circuit.** (a) The simplified circuit for analysis of the voltage noise. (b) The rearrangement of the circuit makes it clear that a simple voltage divider can be used to analyze the voltage noise.

fraction, $\beta = \frac{Z_1}{Z_1+Z_2}$ we can rewrite the above:

$$
\begin{aligned}
e_n &= e_o \left(\beta + \frac{1}{A}\right) \\
e_0 &= e_n \frac{1}{\left(\beta + \frac{1}{A}\right)} \left(\frac{A}{A}\right) \\
e_0 &= \frac{A}{(1 + A\beta)} e_n
\end{aligned}
$$

Unsurprisingly, this final expression takes a familiar form, and this expression could easily be derived from a simple feedback block diagram representation of our circuit with A representing the forward path transfer function, and β the transfer function in the feedback path. Lastly, as a final note, we should emphasize that our expression found above is frequency dependent and only describes the output noise contribution from technical voltage noise at our op amp.

$$e_{0,v}(\omega) = \frac{A(\omega)}{(1 + A(\omega)\beta(\omega))} e_n(\omega) \tag{3.1}$$

The above equation is the main result of this section. We have found how technical noise at our op amp is amplified and filtered by our TIA circuit to give an output voltage.

3.2.3 Current Noise

Having analyzed the voltage noise, we return to Figure 3-5 to analyze how current noise results in output voltage. In Figure 3-8a, we show the equivalent circuit for the analysis of current noise. Like the voltage noise circuit, passive components have been lumped into equivalent impedances, and the noiseless op amp has been replaced by a voltage-dependent voltage source. Additionally, following our superposition approach, the voltage noise source has been set to zero.

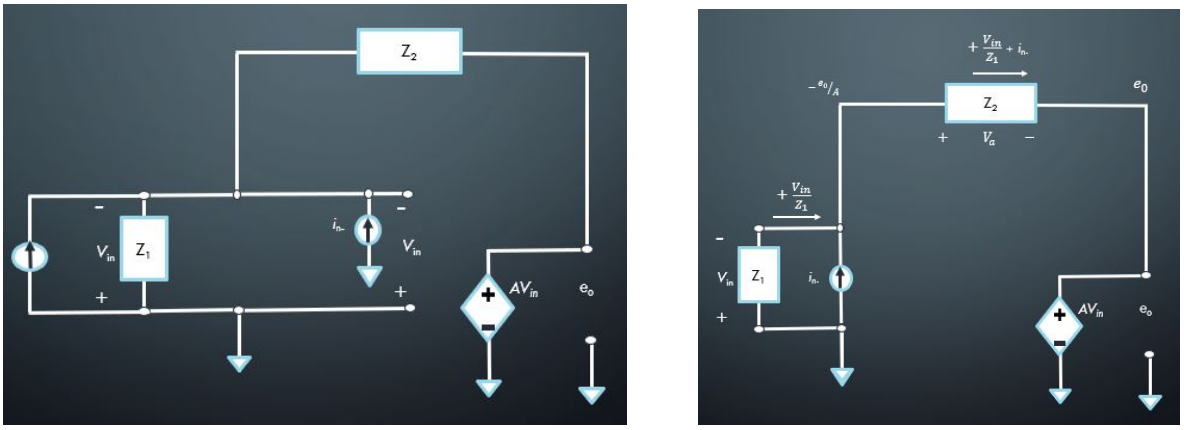

(a) Equivalent Current Noise contribution circuit (b) Phododiode current ignored

Figure 3-8: **Current Noise Circuit**. (a) The simplified circuit for analysis of the current noise. (b) Rearrangement of the circuit with the input current eliminated.

Rearranging the circuit in Figure 3-8a, we find the circuit in Figure 3-8b. Note that in moving to this simplified circuit we eliminated the input current; this followed from our superposition-based approach. (Right now we are only interested in how our current noise from our op amp affects the output voltage.) The circuit in Figure 3-8b can simply be analyzed by applying KCL at the node labeled $-\frac{e_o}{A}$. Applying KCL, we find:

$$\frac{V_{in}}{Z_1} + i_n = \frac{V_a}{Z_2} \tag{3.2}$$

where,

$$V_{in} = \frac{e_o}{A} \quad \text{and} \quad V_a = -e_o\left(\frac{1}{A} + 1\right)$$

Plugging in these equations into Equation 3.2, we obtain an equation that will describe the current noise contribution:

$$\begin{aligned}
\frac{e_o}{AZ_1} + i_n &= \frac{-e_o\left(\frac{1}{A} + 1\right)}{Z_2} \\
e_o\left(\frac{1}{A} + 1\right) + \frac{e_o Z_2}{AZ_1} &= -i_n \times Z_2 \\
e_o\left(\frac{1}{A} + 1 + \frac{Z_2}{AZ_1}\right) &= -i_n \times Z_2 \\
e_o &= \frac{-i_n \times Z_2}{\left[1 + \frac{1}{A}\left(1 + \frac{Z_2}{Z_1}\right)\right]} \\
e_{o,i}(\omega) &= \frac{-Z_2(\omega)}{\left[1 + \frac{1}{A(\omega)\beta(\omega)})\right]} i_n(\omega)
\end{aligned} \tag{3.3}$$

Note that in Equation 3.3 we have made it explicit that the current noise contribution to the output voltage will be frequency dependent. Additionally, we have again written this contribution in terms of the feedback fraction. Equation 3.3 therefore represents the affect of technical current noise in our op amp to our TIA output noise.

3.2.4 Resistor Noise

Thus far we have considered only technical noise from our op amp. Beyond technical noise, we could also anticipate contributions from fundamental noise sources like shot or thermal noise. The dominant contribution from these fundamental noise sources should be thermal noise since thermal in a resistors scales as the square root of the resistance, and in our TIA, there is one very large resistor: the feedback, gain resistance (R_2).

Thermal noise in a resistor is given by the Johnson-Nyquist formula. This formula says that the root-mean-square (r.m.s.) noise voltage in a resistor is given by:

$$e_{o,R} = \sqrt{4k_B T R \Delta f} \tag{3.4}$$

In the above, R is the resistance of the resistor, k_B is Boltzmann's constant, T is the temperature of the resistor, and Δf is the bandwidth under consideration. For a 1-kΩ resistor, this amounts in $e_{o,R}$ of ≈ 4 nV/$\sqrt{\text{Hz}}$. We will use this expression to represent the contribution to the output voltage of the TIA due to noise in the feedback resistor.

3.2.5 MATLAB Program for TIA Predictions

Having found expressions for our three main sources of noise, we can now predict the noise performance of a real TIA design. To aid in these predictions, a Graphic User Interface (GUI) and TIA prediction program was created in MATLAB. The GUI takes in information relevant to the design of a TIA (for instance, the feedback resistance, R_2) as well as technical noise data for a given op amp. The MATLAB program then, with this user-input data, calculates the noise spectral density for our different noise contributions. (To benchmark our program, the results in Ref. [10], found with the OPA111 operational amplifier, were compared to the results of our MATLAB program.)

The first step in using our MATLAB program is importing technical data for a given op amp. Therefore, we begin by looking at the relevant information for an example op amp, the LTC 6241 from Analog Devices Inc. Specifically, in Figure 3-9, we show the voltage noise spectral density, current noise spectral density, and the open loop gain for the LTC 6241. (Data extracted from the datasheet, Ref. [11]). This data will be imported into our MATLAB program to analyze a TIA based on the LTC 6241.

In inputting this data into our MATLAB program, we must ensure that the arrays from the three data sets share the same dimensions. (As seen in Figure 3-9, the frequency axes for these data sets can vary in range.) Firstly, a consistent frequency range is decided, and for data sets that do not fill this range, the data is extrapolated using power functions. We then start by inputting the data into MATLAB. In our GUI, this is done by clicking on either

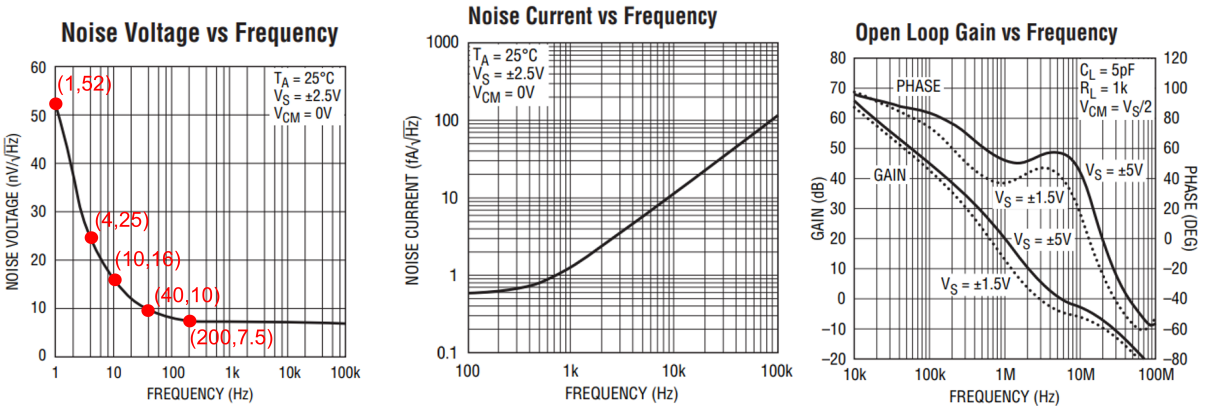

Figure 3-9: **LTC 6241 important parameters**. The voltage noise spectral density, current noise spectral density, and the open loop gain for the LTC 6241.

the "Upload Open Loop Gain" or "Upload Voltage Noise" buttons. A pop up window opens up and asks that the user inputs the first two points; after this, another pop up window asks if the user would like to add another point to concatenate the lines. The user keeps on adding points until the plot has been completed. When uploading subsequent data sets, the interface asks for y values at specific points instead of allowing the user to pick and choose which points to add (see for example, Figure 3-10). This restricts the dimensions of the array and prevents future errors from occurring. (See the annotated points in Figure 3-9 as an example of points that one might upload into the GUI.)

Figure 3-10 displays the main page of our TIA-analysis GUI. On this first page, the user inputs three things: the open loop gain of the op amp (see upper left), the voltage noise of the op amp (see upper right), and the passive component values for the given TIA design (see lower left). A diagram of the TIA circuit and noise model is also shown (see bottom center) to indicate which components entered correspond to the components in the circuit. We should note that, as mentioned previously, R_1 and C_1 are the shunt resistor and capacitor values of the photodiode are necessary to model the photodiode. In practice, R_1 is much greater than 10^6 Ω; therefore, R_1 has minimal impact on the noise analysis. On the other hand, the capacitance of the photodiode, C_1, does have a significant impact on the noise. C_1 can be found in the datasheet of the relevant photodiode, and for the Hamamatsu S1223-01 used in this work, $C_1 = 20$ pF. (The impacts of the values for R_2 and C_2 on the noise will be discussed later.)

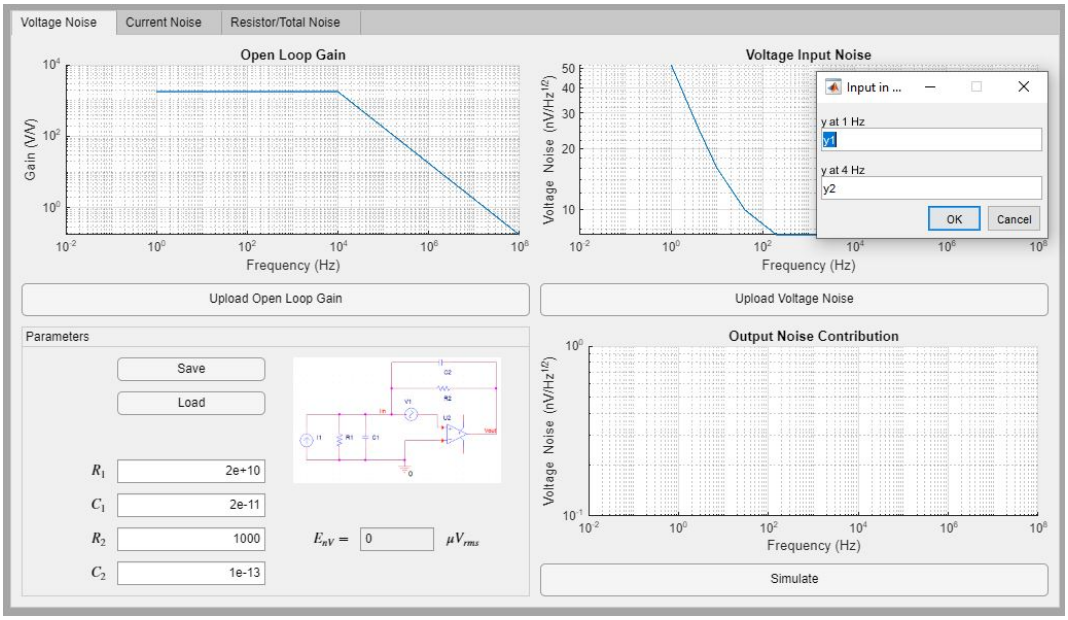

Figure 3-10: **GUI - voltage noise**. After uploading the open loop gain, the user can upload the voltage noise spectral density. When uploading this data, the GUI will prompt the user for noise spectral density values at specific frequencies.

After uploading both the open loop gain and the voltage noise, the user can click "Simulate", and the program will generate a prediction for the output noise spectral density from the input voltage noise. (We should note that, after uploading, the open loop gain and voltage noise data can be saved for later use.)

Following calculation of the voltage noise, the use can click the next page of the GUI, "Current Noise". This page resembles the first page, only the op amp current noise is uploaded and the "Simulate" button there will give the user the noise contribution at the output from the technical current noise of the op amp.

In the last page, "Total Noise" (see Figure 3-11), the user can see the complete predicted voltage noise at the output (in μV_{rms}), as well as a summery of the noise contributions from the voltage noise, the current noise, and the feedback resistor (in $\mu V/\sqrt{\text{Hz}}$). From this window, the user can also adjust the passive component values and see how they affect the noise contributions as well as the expected bandwidth of the circuit. This page also displays a prediction of the output spectral noise density as a function of frequency.

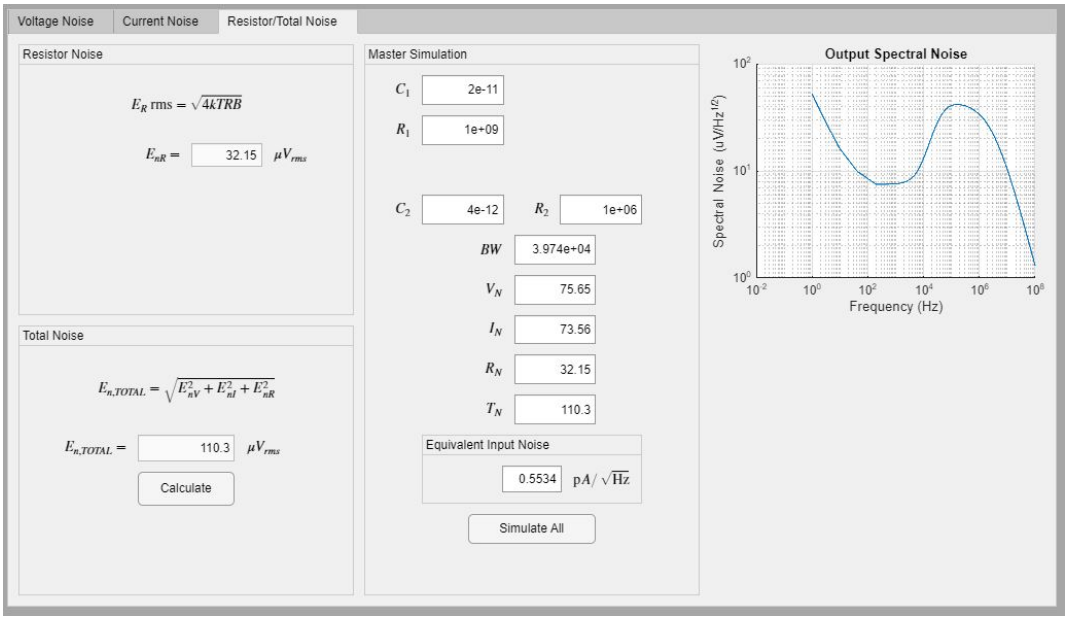

Figure 3-11: **GUI - total noise**. This is an example of the final page of our TIA-analysis GUI. This page gives the total r.m.s. noise, the spectral density contributions from each noise source, and a plot of the total noise spectral density versus frequency.

3.2.6 Initial TIA Design

With a program capable of rapidly analyzing the performance of our basic TIA design with different components, we are now ready to develop an initial design for our application. As noted at the start of this chapter, we aim to have a TIA with a gain of $10^6 - 10^8$ V/A (Ω). Additionally, we are targeting a noise of $\sim$1 pA/$\sqrt{\text{Hz}}$ or below.

Before presenting our initial design, we should make a note concerning the feedback capacitance, C_2. A capacitor will not be placed in our initial design; however, in initial construction, we will use a solder-less breadboard that possesses parasitic capacitance. As shown in Figure 3-12, the row-to-row capacitance in a standard solder-less breadboard is around 2-3 pF [12]. In our layout, the inverting input and the output of the op amp are in adjacent rows; this leads to an unavoidable capacitance in our feedback network which will add to the other parallel parasitic capacitance of our feedback resistors. These capacitors will directly impact the bandwidth of our device and so must also be considered in our predictions.

In our initial design, we will use the LTC 6241 operational amplifier from Analog Devices Inc. This op amp is a FET-input op amp with extremely low bias current and low noise.

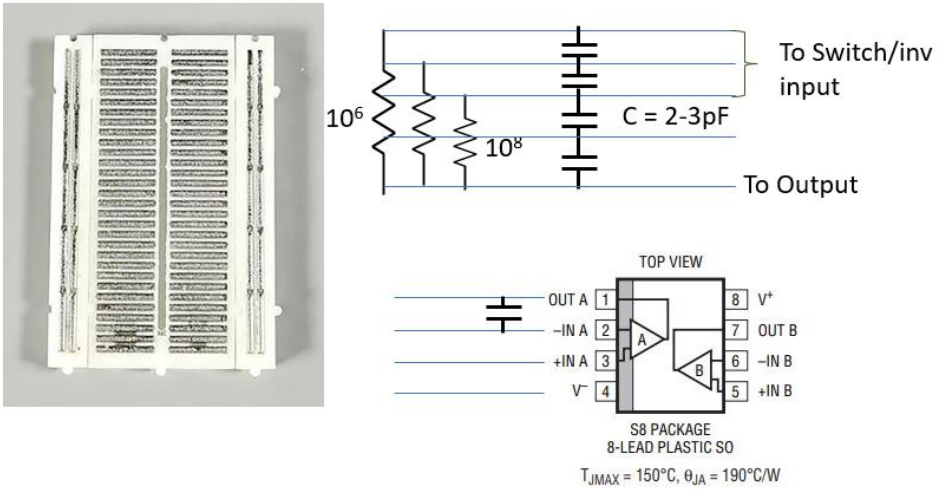

Figure 3-12: **Parasitic capacitance in a solder-less breadboard**. The row-to-row capacitance in a standard solder-less breadboard is around 2-3 pF. The op amps that we will use have the inverting input one row away from the output. This leads to an unavoidable feedback capacitor, C_2.

(The LTC 6241 op amp is recommended for TIA applications.) The initial design will consist of the simple circuit shown in Figure 3-13. The circuit will be built on a breadboard to check for correct op amp operation and simplified initial testing. To provide the necessary gain, we will use three different feedback resistors for 10^6, 10^7, and 10^8 Ω. (In Figure 3-13 only a 100 MΩ resistor is displayed.)

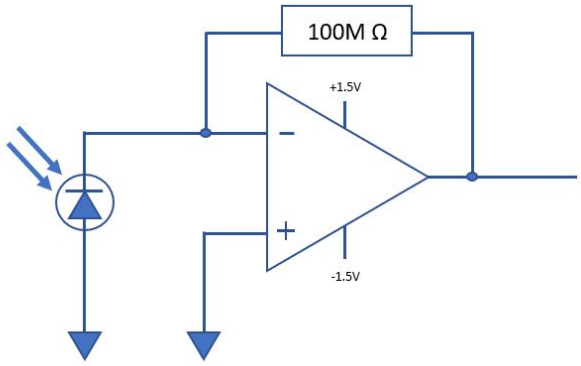

Figure 3-13: **Initial design**. The op amp being used will be the LTC 6241HV with a Hamamatsu S1223-01 photodiode at its inverting input and a high resistance feedback resistor for gain.

Using our TIA-analysis program, we calculate the expected performance of the TIA. We

perform this analysis for all three gains. The results are included in Figure 3-14.

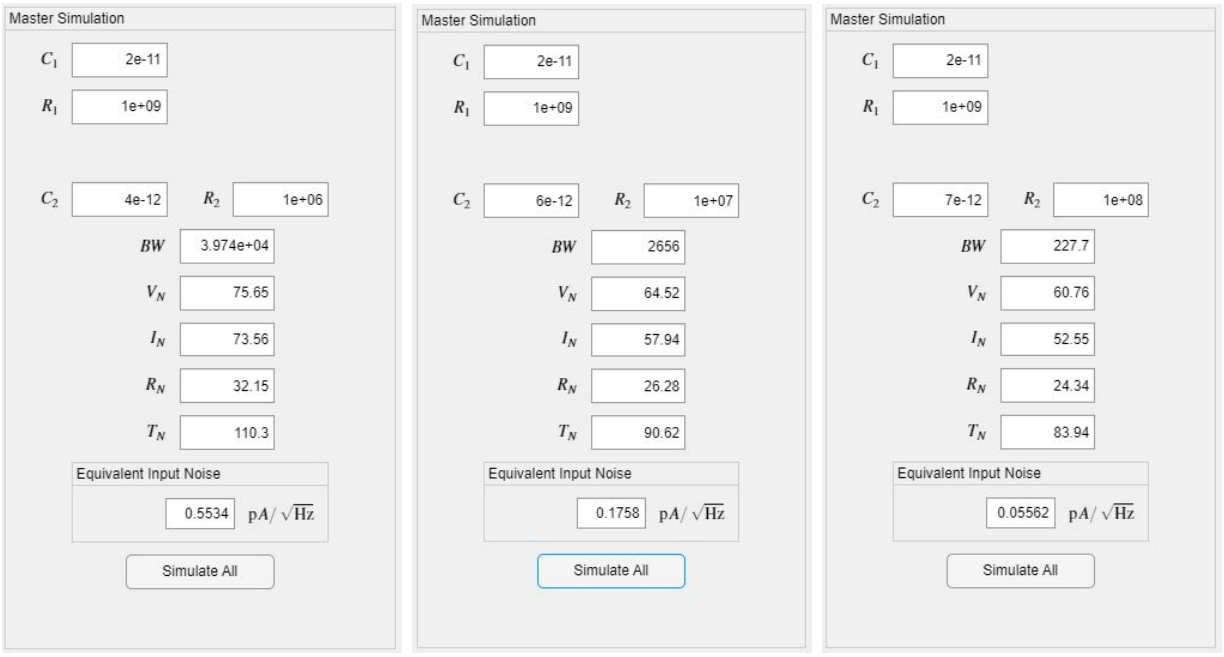

(a) 10^6 V/A (b) 10^7 V/A (c) 10^8 V/A

Figure 3-14: **Matlab bandwidth predictions** - Three important predictions are made here. (a)From the parasitic capacitance discussion, 4pF is assumed to be in the feedback network along with a feedback resistor of 1MΩ. Around 40kHz of Bw is predicted along with $0.55\text{pA}/\sqrt{Hz}$ of equivalent input noise. For the other Gain selections, (b) 2.63kHz Bw with $0.176\text{pA}/\sqrt{Hz}$, and (c) 230Hz Bw with $0.06\text{pA}/\sqrt{Hz}$

Note from the predictions that we are easily able to achieve our desired noise specification. Each amplifier provides noise well below 1 $\text{pA}/\sqrt{\text{Hz}}$. Additionally, note that the feedback capacitance varies slightly from amplifier to amplifier. All of the values for C_2 are reasonable considering the parasitic capacitance of the breadboard. Furthermore, C_2 increases slightly from the 10^6 to 10^8 V/A amplifiers as the feedback resistors in these different amplifiers was positioned slightly differently; in the highest gain design the leads of the resistor were placed slightly closer together, likely leading to a higher feedback capacitance. Ultimately, as we will see in the following section, these parasitic C_2 values lead to predicted bandwidths for the TIAs that are very close to the measured values.

In our design we will use a specific variant of the LTC 624, the LTC 6241HV. This op amp requires a voltage supply (V_s) anywhere from 2.5V to 12V. For portability (and to potentially eliminate power supply noise), in our initial design we elect to operate our amplifier at ±1.5

V. This power can easily be provided by two AAA batteries.

The build of the initial design is shown in Figure 3-15. A two-AAA battery pack (Figure 3-15a white wire) was used for our power supply. A double-pole single-throw (DPST) switch was used to turn the op amp off and on, and the photodiode was place in the center on top of a PCB mount to allow the photodiode to sit higher than the rest of the components (Figure 3-15b). A bottom case was 3D printed to house both the breadboard and the battery pack. A twisted pair of yellow and white wires carried the output of our amplifier.

(a) Battery pack

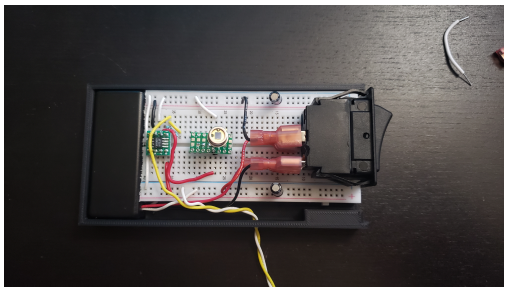

(b) 3D printed bottom case

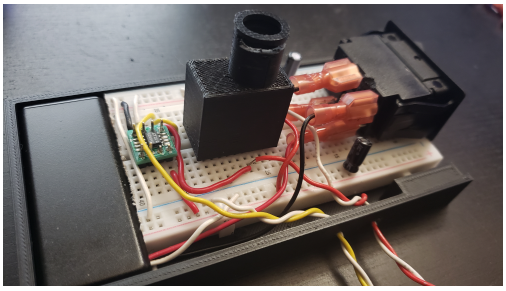

(c) Photodiode aperture

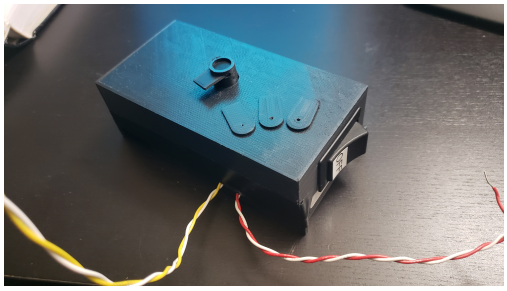

(d) Top cover added, with step-varying apertures on hand.

Figure 3-15: **Initial TIA build**. The initial build had the circuit build on a breadboard, and the photodiode, battery pack, and circuit mounted in a 3D-printed enclosure.

In order to restrict excitation by ambient light, the photodiode was encased in its own box (Figure 3-15c). The top cover of the circuit fit nicely around this (Figure 3-15d). The photodiode enclosure was made with a slit in the cylindrical extrusion. This slit allowed various apertures to be inserted and enabled us to further restrict how much light could reach the detector.

Lastly, in our initial build, a twisted pair of red and white wires were added into our circuit as shown in Figure 3-15. These wires are connected to the input of the op amp. They were used in the testing (as described in the following section) to measure the current that

the photodiode is supplying before reaching the op amp. This measurement was made with a picoammeter, and, as will be described in the following section, enabled us to calibrate the gain of our TIA.

3.3 TIA Testing

With an initial TIA design and an initial build, we are now ready to consider the testing of our TIA. In this section, we will first describe our initial testing efforts. The initial testing indicated that we had a functioning circuit; however, it also revealed challenges associated with characterizing a high-gain, low-noise TIA. Informed by this initial testing we took efforts to mitigate the effects of outside noise. We describe these efforts following the discussion of our initial testing. After limiting the impact of outside noise and developing a more reliable experimental platform, we proceeded to make gain, bandwidth, and noise measurements of our initial TIA. We present these results in this section.

3.3.1 Initial Tests

The experimental arrangement for our initial tests is shown in Figure 3-16). In the initial tests, a cell phone flashlight was held at a fixed distance from our TIA. The TIA was at first switched off, and the input current to the TIA was bypassed to a picoammeter (Keithley 486). The picoammeter was used to measure the input to the TIA (for gain calibration). After measuring this input, the picoammeter was disconnected, and the TIA was switched on. All tests were performed with the room lights off.

Before our first tests, we needed to establish a fixed reference for our input current measurements. In our tests, the picoammeter was used to first measure the current produced by the photodiode with the room lights off. However, to ensure that our picoammeter reading truly corresponded to the photodiode current, we recorded a baseline current before turning on the flashlight. Under these baseline conditions, the picoammeter output reading was "zeroed", and following this referencing, the flashlight was turned on and the resulting current was measured. To ensure consistency and minimize the impact of drift, our baseline was re-established after each new measurement to account for any minor shifts in TIA displacement.

Figure 3-16: **Experimental setup for initial design** - The distance and position of the flashlight and the TIA is kept fixed. The oscilloscope is disconnected to record current readings. Then, the picoammeter is disconnected while the oscilloscope is connected, and the TIA is switched on to record the output voltage.

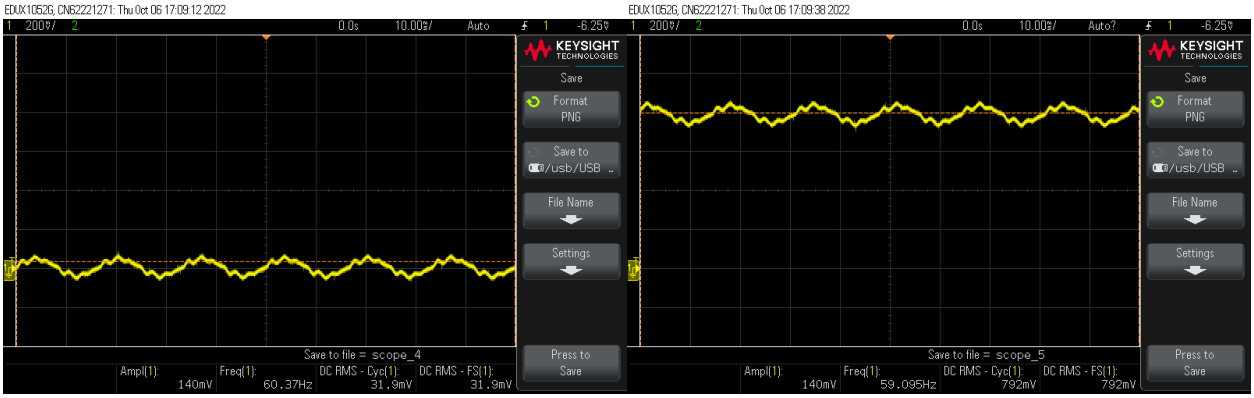

(a) Flashlight OFF reading - Background noise

(b) Flashlight ON reading - DC RMS value was used to calculate TIA gain.

Figure 3-17: **Initial TIA design output example**. (a) The output of the TIA with the flashlight off. (b) The output of the TIA with the flashlight on. The trace has jumped to 792 mV with 8 nA of current, corresponding to a TIA gain of 0.99×10^8.

With our picoammeter appropriately reading the photodiode current, we began our first tests. In these tests, we measured the performance of our initial design with a 100 MΩ feedback resistor (and an expected transimpedance gain of 10^8 V/A). We began with a completely shut aperture. This measurement was made to see if the TIA could record any light coming through seams or openings in the 3D-printed enclosure. When switching the

flashlight on and off, a consistent 21.5 pA was read on the picoammeter. At the output of our TIA, the voltage reading went from 22.6 mV to 23.1 mV. This rise in voltage is slightly smaller than expected and is likely too close to the background noise to make for a reliable measurement. Next, the aperture was opened slightly by inserting a different slit. In Figure 3-17, we show an output reading on the TIA of 792 mV with an input current of 8 nA (as read on the picoammeter). This corresponds to a transimpedance gain very close to the expected value of 10^8 V/A.

Following these first measurements, three more initial measurements were made in the same manner. These results are included in (Figure 3-18). These first results indicated that our TIA was performing with a gain close to the expected value. However, the gain was drifting by larger than expected amounts.

After these preliminary measurements, it was clear that there were two main deficiencies in our measurements. Firstly, there was an issue with 60-Hz pickup. This 60-Hz signal is clearly evident in our measurements in Figure 3-17. Secondly, our measurement apparatus was too susceptible to drift. Small movement in the TIA (resulting for example from plugging or unplugging the oscilloscope from the output) could slightly reposition the amplifier and photodiode and cause a change in the output signal. In the following section, we will describe how we addressed these shortcomings.

Experiment	1	2	3	4
pA Reading	8.0 nA	4.0 nA	1.3 nA	630 pA
Flashlight OFF	32.1 mV	24.7 mV	25.4 mV	24.7 mV
Flashlight ON	792 mV	418 mV	127 mV	66.3 mV
Transimpedance Gain	9.90E+07	1.05E+08	9.78E+07	1.05E+08

Figure 3-18: **Initial gain results** - A quick measurement testing a short range of current was taking quickly test the validity of the current testing environment.

3.3.2 Mitigating Outside Noise

As identified in our initial tests, 60-Hz pickup posed a significant challenge in testing our high-gain TIA. This 60-Hz signal derives from the power distribution systems surrounding the

amplifier. As shown in subsection 3.2.6 Figure 3-17, this noise would routinely reach levels of $>$ 140 mVpp in our initial testing. (The highest recorded value of this pickup was $\sim$400 mVpp.) As a first effort to decrease this pickup, we wrapped multiple layers of aluminum foil around our device. Aluminum foil is far from the ideal choice for this shielding from low-frequency pickup; however, after grounding the foil to the internal circuitry, the 60-Hz pickup reduced to $<$ 20 mVpp. The foil shielding and a representative pickup measurement are shown in Figure 3-19b.

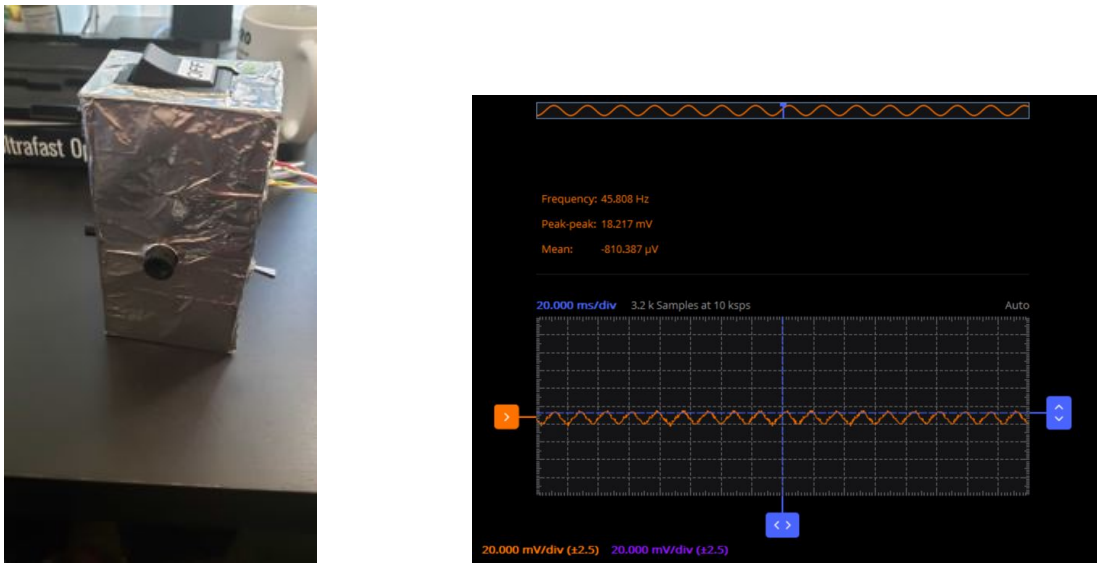

(a) Aluminum foil shielding

(b) Oscilloscope - 60Hz

Figure 3-19: **Shielding and 60-Hz pickup**. (a) The aluminum foil shielding. (b) An oscilloscope trace showing the output of the TIA. Note: the 60-Hz pickup has been reduced from the hundreds of mVpp to around 16-18mVpp.

The 60-Hz pickup observed in Figure 3-19b is sufficient for our first TIA implementation. However, we should note that there are two clear paths to further suppressing this pickup. First, upgrading our shielding to a thicker, grounded metallic box will likely further reduce the effects of pickup. Secondly, the layout and wiring of the TIA should be adjusted. Care should be taken to identify and eliminate potential ground loops and excess wiring.

Beyond pickup problems, our initial tests also indicated the need for a new, more stable test apparatus for our TIA. For the measurements presented in the subsequent subsections, we used a new experimental arrangement, as shown in Figure 3-20. In the new setup, the cellphone flashlight was replaced by a red LED. This change was made for a better control of

our light source. (It was also foreseen that the bandwidth of the TIA will have to be tested, hence a function generator would have to be added to drive our light source at different frequencies.) Additionally, our setup uses a new electronic interface; specifically, we used an ADALM 2000 from Analog Devices Inc., along with the software named Scopy. The ADALM 2000 works as an oscilloscope, a function generator, and a power supply. The power supply was used for gain measurements, while the function generator was be used to test the bandwidth of the TIA.

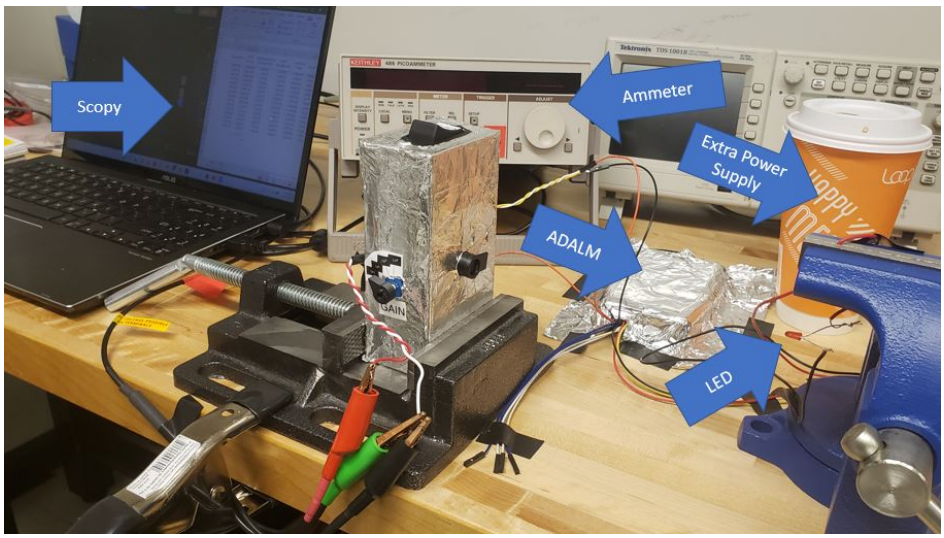

Figure 3-20: **Experimental setup for gain and bandwidth measurements**. This setup allowed for a more permanent spot for testing. Both the LED and the TIA were locked in place using bench vises and the ADALM was covered since it illuminated a blue LED when turned on.

3.3.3 Gain Measurements

In this subsection, we report the measurements of the gain of our TIA. We should note that we will test our basic TIA design with three different feedback resistors; these resistors were installed in the amplifier and could be toggled with a switch. This enabled us to select a TIA gain of $\sim 10^6$, $\sim 10^7$, or $\sim 10^8$ V/A. The layout of the switchable gain amplifier is shown in Figure 3-21.

In our gain measurements, we took a similar approach to the methods discussed in subsection 3.2.6. First, the photodiode was isolated from the TIA via the installed switch,

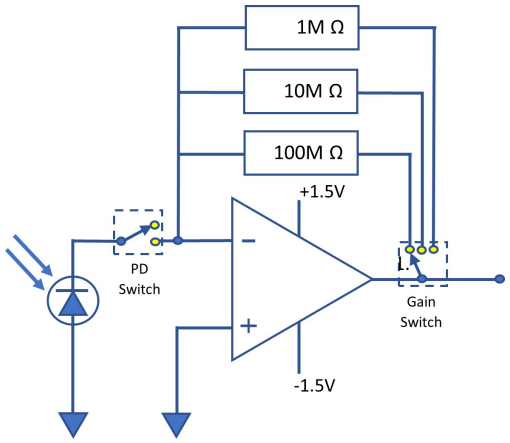

Figure 3-21: **Selector gain circuit**. We installed three feedback resistors in our amplifier so that we could select different gains for our TIA.

Gain Switch	Input Current	Background Vout (Flashlight OFF)	Vout (Flashlight ON)	Calculated TI Gain	% Error
1.00E+08	1.9E-11	-1.E-03	1.3E-03	1.21E+08	21.05%
1.00E+08	6.2E-11	-1.E-03	5.2E-03	1.06E+08	6.45%
1.00E+08	7.8E-11	-1.E-03	6.9E-03	1.01E+08	1.28%
1.00E+08	1.15E-10	-1.E-03	1.07E-02	1.02E+08	1.74%

Figure 3-22: **Gain measurement sample** - This is only but a small fraction of many different input current and output voltage measurements taken.

and a baseline current was established by turning off both the LED and the room lights. The LED was then turned on and the current flowing out of the photodiode was measured on the picoammeter and recorded and labeled as "input current", as shown in the sample data table in Figure 3-22. Next, the picoammeter was disconnected, the photodiode bypass switch was closed, and the TIA was turned on. By turning the LED on and off, we subtracted the background offset from the signal being amplified and calculated the gain of our amplifier. This procedure was repeated while increasing the brightness of the LED or while adjusting the aperture on the device. Once the amplifier saturated, the gain was reduced and the process was repeated until all three gains were tested.

In Figure 3-23, the results of our gain measurements are shown for each of the three gains. From this graph, we can see the approximate integrated noise floor of each amplifier setting. Clearly, at a critical current, the amplifier gain deviates from the design; this value is approximately where the input signal dips below the integrated input noise level. The graph

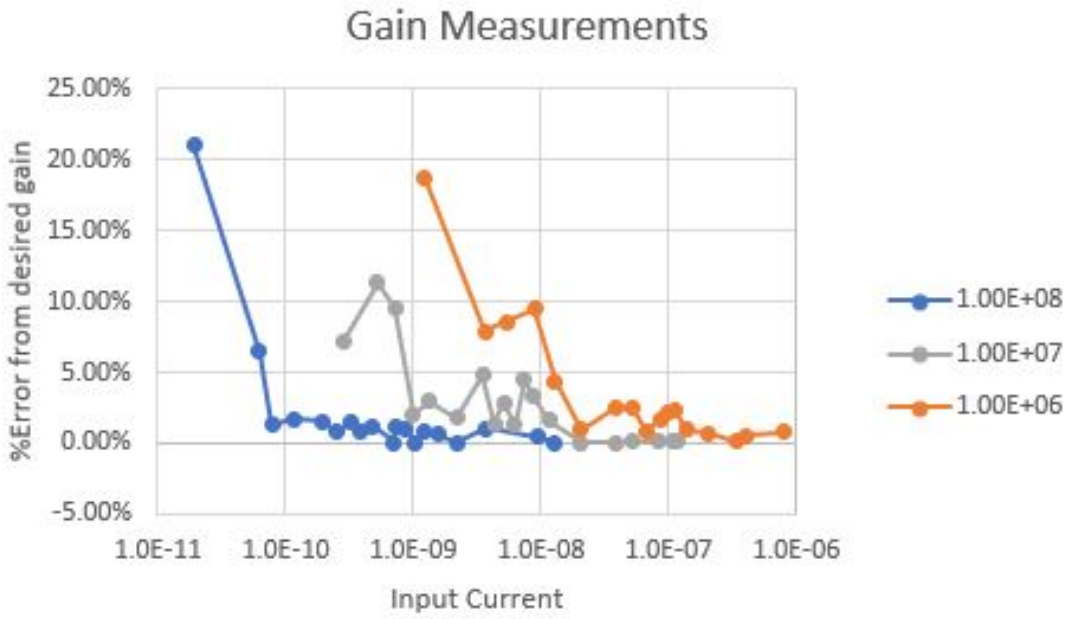

Figure 3-23: **Full gain measurements** - Each Gain setting has around 20 measurement points. The currents chosen to measure a gain are not equally spaced nor equally logspaced. DC Voltage on the LED was step increased with the steps decreasing in value as higher voltages were reached due to the nonlinear response of the LED.

shows that when the gain selector switch is placed on 10^8 V/A, the TIA can read currents as low as ∼80 pA before reaching the noise floor and as high as 10 nA before saturating, all within a 3% gain error. The next gain down has the same range of 10^8 V/A, but shifted upwards by one order of magnitude, which is to be expected. The same can be said for the 10^6 V/A gain.

The minor fluctuations seen in the 10^7 V/A gain are mostly likely due to the lack of an appropriate aperture size for this gain measurement. The aperture used during this test had to be placed halfway in, which made the TIA very sensitive to mechanical disturbances when disconnecting and reconnecting the picoammeter. This goes to show how sensitive the amplifier can be in reading these small changes, while still remaining within a 5% gain error window.

3.3.4 Bandwidth Measurements

As will be discussed in chapter 4, we will require our TIA to respond to alternating signals with frequencies on the order of 100-1000 Hz. Specifically, in our our autocorrelator, we will use an optical chopper and lock-in detection. To use this chopper, our amplifier must have sufficient bandwidth to keep up with the chopped signal. In this subsection, we characterize the bandwidth of our TIA.

To measure the TIA bandwidth, we will modulate our red LED with a known sinusoid and look for a response to this sinusoid on our TIA. Prior to this measurement, we first measured the bandwidth of our LED-driving system. For this measurement, a reference photodiode (Thorlabs PDA100A2) with bandwidth >10 MHz was used. Our setup is shown in Figure 3-24. We aimed to confirm that the LED can be driven at different frequencies while maintaining a constant peak-to-peak voltage. Driving the LED with a sinusoidal signal at different single frequencies allowed us to create a frequency response plot and look for the -3 dB point, to identify the bandwidth of the LED-driving circuit. We will ultimately find the bandwidth of the TIA in a similar manner.

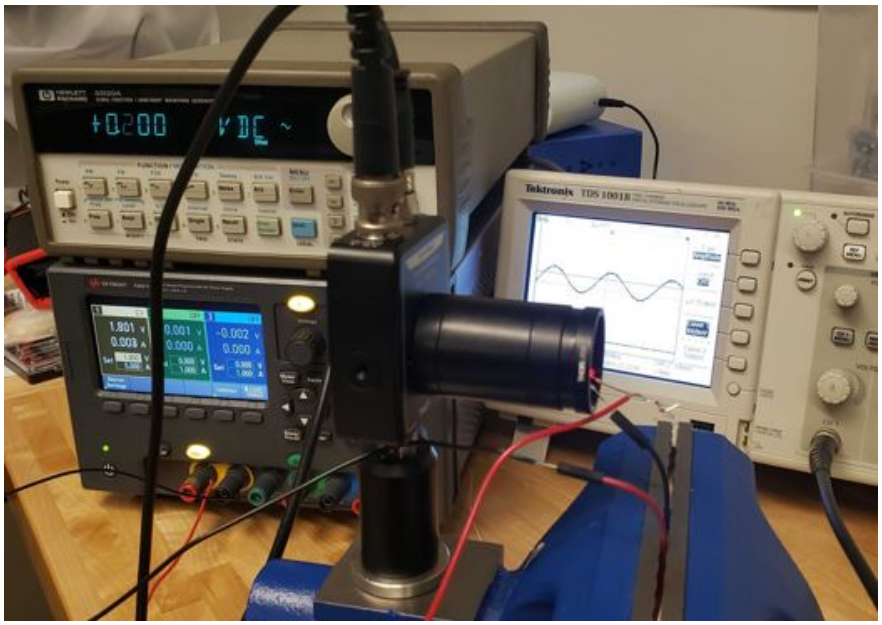

Figure 3-24: **LED BW test** - Each Plot has around 10 measurements done per decade. These measurements only deviated by around 1% of a mean value. There was no need to take multiple measurements for any given point.

In the LED-driving circuit, the nonlinear I-V characteristic of the LED was not overlooked. If a large signal drives the LED, the current, and emitted light, of the LED will respond in a nonlinear way. This means that the voltage produced by the light sensor will carry multiple frequencies besides the driven frequency. To overcome this difficulty, the LED was biased at a moderate DC level, and a function generator was used to provide a weak AC signal; this allowed us to create a single-frequency modulation of our LED output. The frequency of this output was swept, and the bandwidth of our LED-driving circuit was found to be ∼290 kHz, significantly larger than the expected bandwidth of our TIA (see subsection 3.2.5).

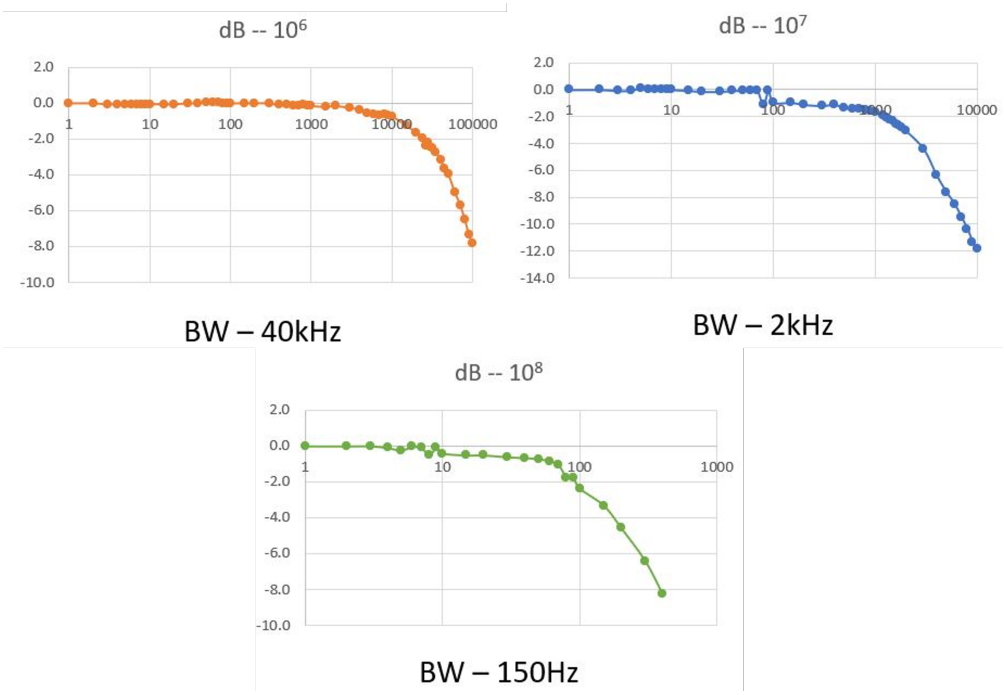

Figure 3-25: **Bandwidth measurement results** - Each plot contains around 10 individual measurements done per decade to track how well the TIA responded when an LED shined and driven with a function generator at different increasing frequencies. When the Gain selector is placed at 10^6, it's BW was around 40kHz. 2kHz at 10^7, and 150Hz at 10^8 agreeing well with our previous predictions.

To test the bandwidth of our TIA, the same procedure was used as for testing the LED-driving circuit. This procedure was repeated for our three different gains. In Figure 3-25 the results are presented. Overall, these experimental results closely match our predicted TIA performance (see subsection 3.2.5, Figure 3-14).

3.3.5 Noise Measurements

Characterizing the noise of our TIA is done using lock-in techniques. This technique requires a lock-in amplifier that monitors and calculates the root-mean-square (r.m.s.) noise at a programmed referenced frequency. We utilize the SR830 DSP lock-in amplifier (Stanford Research Systems), which provides its own adjustable internal reference frequency.

Typically, lock-in amplifiers are used to find the amplitude and phase of signals buried within noise. As will be discussed in chapter 4, a modulated signal created after a "chopper" will consequently produce a signal at the chopper frequency. The generated second harmonic modulated signal that arrives at the detector will be susceptible to the surrounding natural noise. We then tell the lock in amplifier which frequency to look at, and the instrument will lock in to the frequency of this signal and retrieve its amplitude and phase.

To help visualize this technique, Figure 3-26 has been made to model an example. A signal of known frequency (5 kHz) has been infected by random noise ranging from 10 Hz to around 15 kHz. The time domain plot in the bottom left demonstrates what you would see in an oscilloscope when trying to measure the signal voltage. To the right of these plots is the power spectrum of both the noise and the signal combined. Within this plot, we can clearly see a 5 kHz signal embedded within all the noise. By applying a narrow bandpass filter at this central frequency with a high enough slope, the signal can be successfully recovered.

Although this signal retrieval technique is used in our autocorrelator, it is not used to benchmark our TIA, as we are not trying to find a signal in this scenario. However, finding the noise spectral density of our TIA is done in a very similar manner. Rather than setting the lock-in amplifier to look for the amplitude and phase of a signal, we set it to calculate the real and imaginary noise values within the narrow bandpass filter's bandwidth. Using the internal adjustable reference frequency, we can sweep through different frequency to build up a rough noise spectral density vs frequency plot where the y-axis is the r.m.s. voltage as calculated by the magnitude of the real and imaginary values displayed on the instrument divided by the root bandwidth of the bandpass filter (Equation 3.5).

$$V_{\text{rms}} = \sqrt{X^2 + Y^2}/\sqrt{BW} \tag{3.5}$$

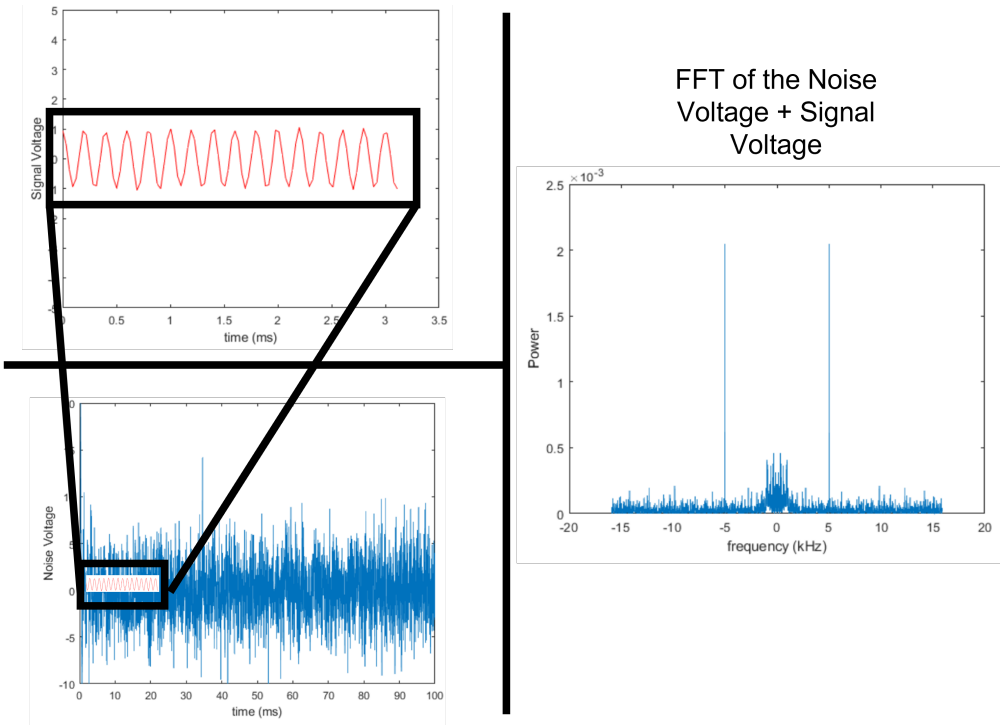

Figure 3-26: **Signal Retrieval** - An example showing how a signal barried in noise can be retrieved by applying a very narrow bandpass filter at the signals frequency. This technique is known as lock-in detection, and is a technique used for both characterizing the TIA's noise, and to detect a weak signal in an autocorrelator.

The bandwidth of this filter, is dependant on the slope of the filter and the time constant selected at the interface. Higher slopes give a higher resolution, but require a longer wait time.

The noise measurement experiment performed was first done with the PIN photodiode switch turned off to measure the noise of the op amp, then turned on to measure the noise of the circuit experiencing the noise produced by dark currents. This gives an idea of the noise floors we should expect at different gains if we were to minimize light pollution. The slope was selected at 24 dB/oct with a time constant of 100 ms. Results of the experiment are shown in Figure 3-27 and Figure 3-28.

Each point in the plot corresponds to ten measurements recorded and averaged out. The two displayed noise values (real and imaginary) update every second, making it difficult to record a single measurement. Furthermore, these values deviated by less than 10%, hence the requirement of taking a few measurements and averaging them out. At a given time,

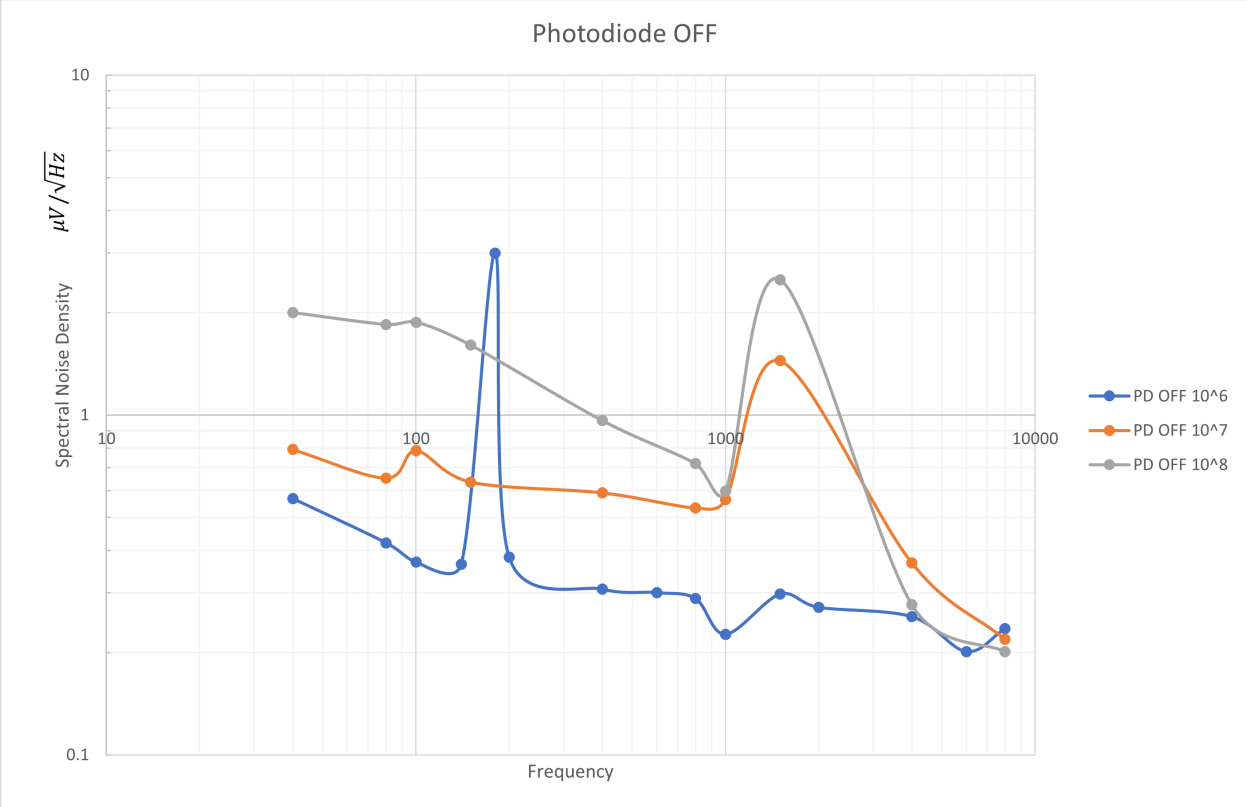

Figure 3-27: **Noise measurement PD off** - Each point contains 10 measurements averaged out due to deviation that were close to 10% of the obtained average.

the X value and the Y value correspond to one another, making it necessary to record both values at the same time. To record these measurements, it was necessary to take 10 pictures spanning across 2 seconds each. The magnitude of each individual picture was calculated and divided by the square root of the bandwidth (0.78 Hz) then averaged out to obtain a single value for the referenced frequency used. The time constant (100 ms) was chosen to save time during measurements while keeping a reasonable resolution.

Observing the values in the lower frequencies when the photodiode is on and performing a simple calculation estimate will show these results closely match to those from the MATLAB simulations in Figure 3-14. Taking the first point in the PD ON 10^7 trace the equivalent input noise in terms of current would be:

$$I_n = (1\ \mu\text{V}/\sqrt{\text{Hz}})/10^7 = 0.1\ \text{pA}/\sqrt{\text{Hz}}$$

The hump at the higher frequency was also predicted (see Figure 3-11). However, in the

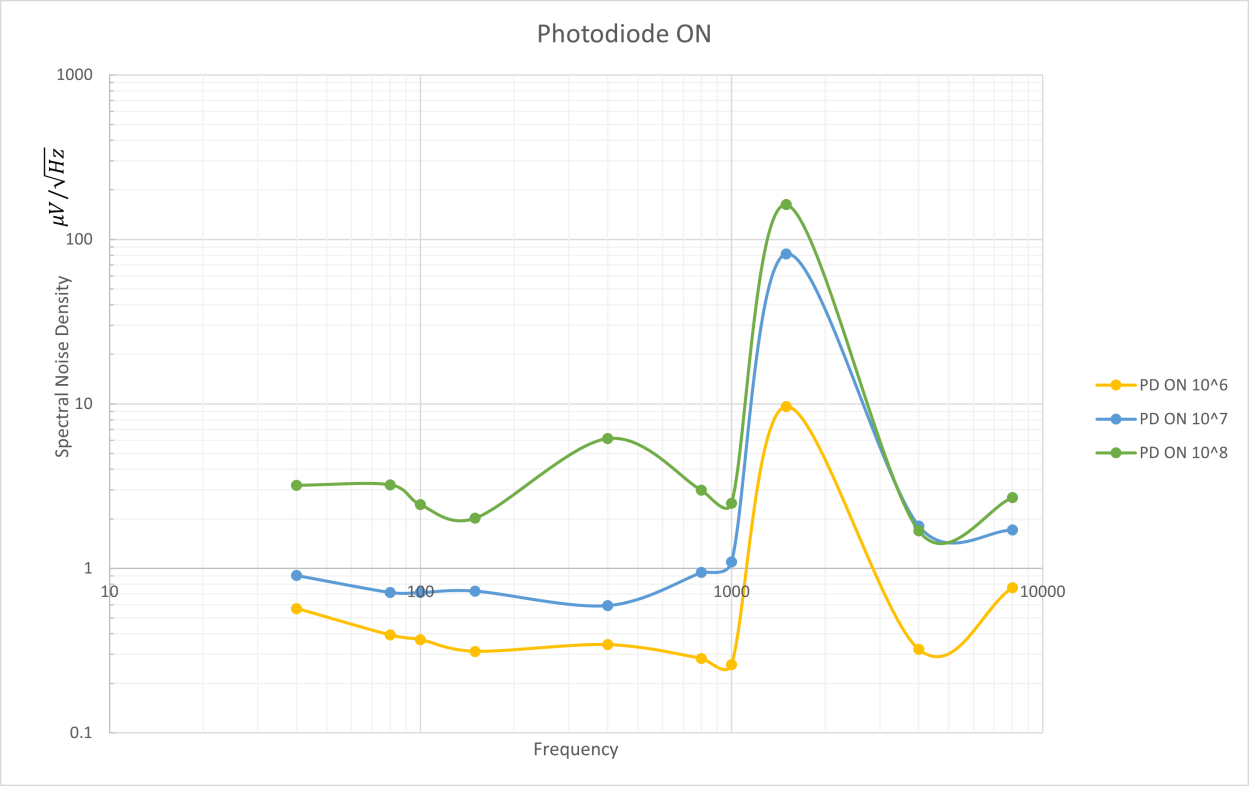

Figure 3-28: **Noise measurement PD on** - By turning on the photodiode, the dark currents provided by the photodiode start become visible as noise. Hence why we see an increase in the overal curve when compared to when the photodiode is off.

experimental measurement, the hump is seen at a lower frequency. More experimental data at strategically chosen frequencies would help shed more light on this phenomenon. Nevertheless, a lowpass filter could be added to remove the higher frequency noise. Another great discussion in [13] employs different techniques at the front-end of a TIA further decrease noise while maintaining high bandwidth.

Chapter 4

Autocorrelation Experiments and Results

In this final chapter, we describe the optical systems that we have built to measure our ultrafast, second harmonic pulses. Specifically, in this chapter, we will describe the construction of an interferometric autocorrelator. We will overview the optical layout of the interferometer, describe the alignment procedure, and, finally, we will present our initial results from this tool. Our results will indicated limitations of our pulse measurement system, and in a final section of the thesis we will discuss next steps. In particular, we will describe how we will modify our current pulse measurement system into an intensity autocorrelator, which will enable better filtering, higher signal, and, eventually, modification to more advanced pulse measurement schemes.

4.1 Inteferometric Autocorrelation

In Chapter 2 we described basic ultrafast pulse measurement schemes, and we concluded that interferomteric autocorrelation was the most informative of the fundamental techniques based on autocorrelation. In this section, we describe the construction, alignment, and use of an interferometric autocorrelator for our second harmonic generation from our Cr:ZnSe/S laser system.

4.1.1 Optical Layout

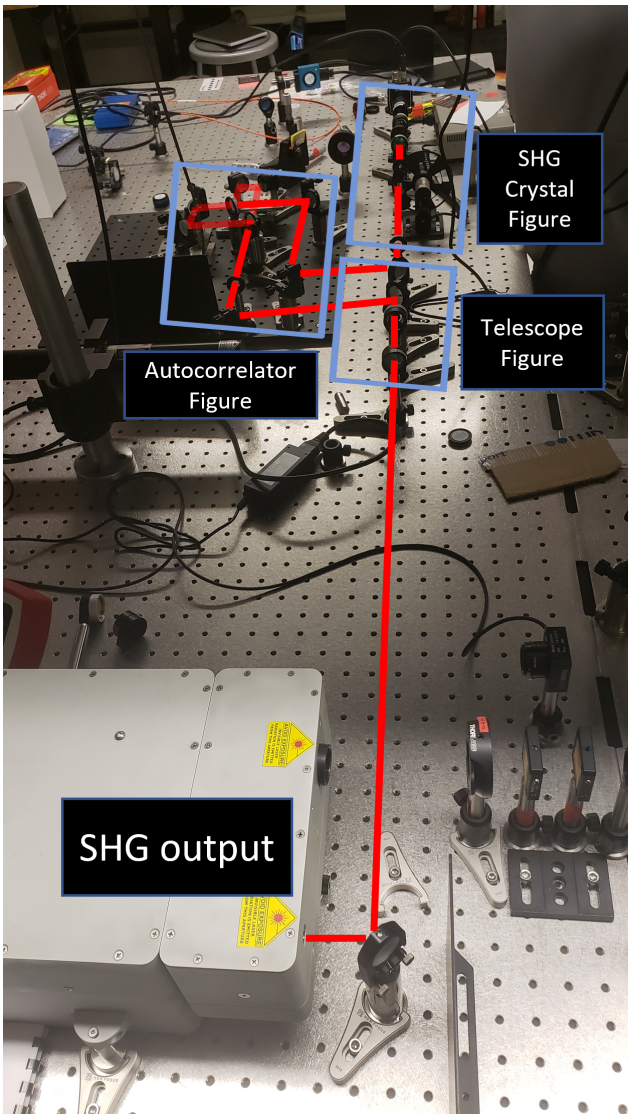

Figure 4-1: **Optics table** - The laser system has two outputs, one of which has been covered, while the other (SHG) is sent through a telescope, steering mirrors, the autocorrelator, another set of steering mirrors, a "chopper", then focused onto the BBO crystal, gets recollimated, and finally sent to two filters that should be able to attenuate the 1.2micron beam to a negligable value.

The optical layout begins with the inspection of the second harmonic output beam with a infrared laser viewing card. These photosensitive cards have active areas which emit visible radiation when illuminated by particular infrared wavelengths. The card enabled the alignment of the beam while also giving us an idea of how wide the beam is the spatial domain. After careful considerations, which we will discuss in this chapter, our optical setup

was built as shown in Figure 4-1. This figure will be broken down into three sections: the telescope, the autocorrelator, and the second harmonic generation. A condensed schematic of our optics table is shown in Figure 4-2.

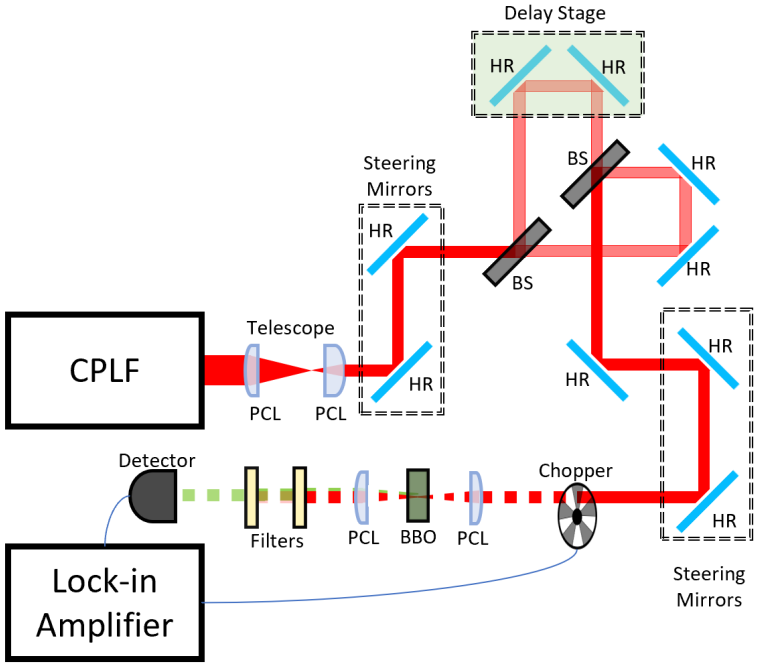

Figure 4-2: **Interferometric autocorrelation schematic** - A condensed schematic of our setup is shown which was used to obtain some initial results for interferometric traces.

Initial inspection of the SHG output using the viewing cards showed that the beam was very large, ∼2 cm in diameter. For proper alignment and overlap, the beam is required to reflect off mirrors while avoiding clipping near the edges of mirror. To compensate for such a large beam, two Anti-Reflection (AR) coated plano-convex lenses (PCL) were used to reduce the beam to roughly 0.4× its original size. A top view of this section can be seen in (Figure 4-3), while Figure 4-2 shows the orientation of these lenses. The collimated beam enters the spherical side of the PCL to reduce spherical aberrations (which correspond to the spread of the focal point due to irregularities in the optical surface.) The next PCL is placed, with the flat side first, after (but closer to) the focal point of the first PCL to re-collimate the beam. The first PCL is the LA1257-C from Thorlabs with a focal length

of 75 mm, followed by the LA1805-AB with a focal length of 30 mm. To re-collimate the beam, the ideal distance between these to lenses would be the added value of both focal lengths, 105mm. The reduction in beam size will therefore be, $30/75 \approx 0.4$ of the original size. Figure 4-4 helps visualize this reduction in beam size produced from an open source website that provides interactive simulations [14].

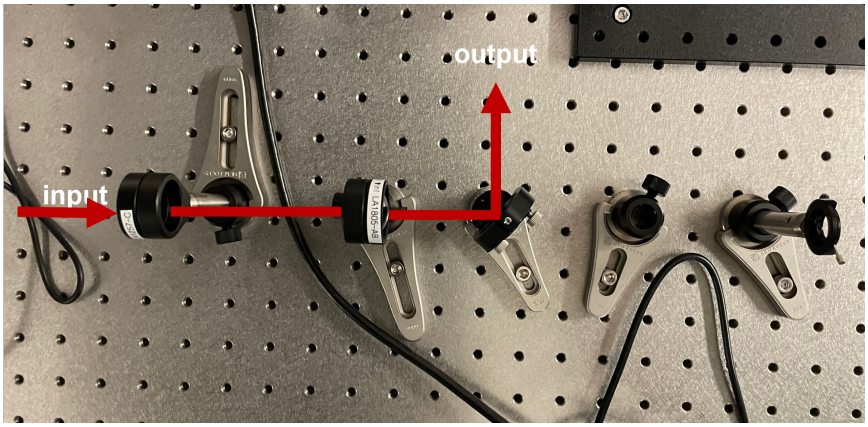

Figure 4-3: **Top view of telescope**

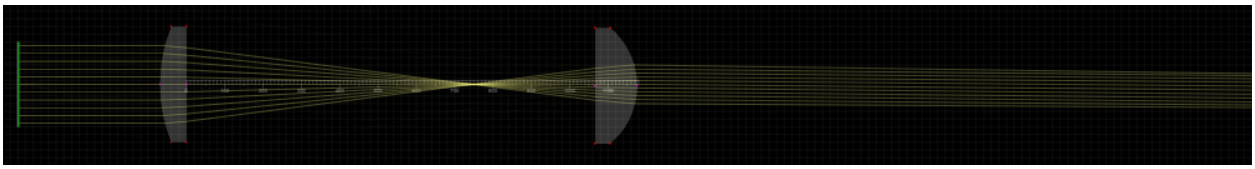

Figure 4-4: **Ray optics simulation** - This visually shows a beam shrinking to about 0.4x its original size using a 75mm plano-convex lens with a 30mm plano-convex lens

Leaving the telescope, our beam now goes through what are called "steering mirrors". These mirrors help "walk" the beam into alignment and will be further discussed in the subsection that follows. After the steering mirrors, the beam propagates into the next section: the autocorrelator.

Within the autocorrelator, the beam will pass through two 50:50 beamsplitters (BSs) that are compatible with wavelengths in the range of 1000-2000 nm. These beamsplitters (Thorlabs UFBS5052) are specially designed for ultrafast pulses: the beamsplitters present a small and precise group delay to both reflected and transmitted waves. Reflected waves experience 15-20 fs of group delay, and the transmitted beam experiences a group delay of around 23-34 fs. Furthermore, the total group delay experienced by a wave in the auto-

correlator is balanced by the geometry of the autocorrelator. Considering one single path, the beam that will travel to the delay stage for instance, we see that the beam will be first reflected as it passes the first BS, then transmitted as it passes the second. Also, following the second path, the second beam will experience transmission in the first BS and reflection at the second. This means that the overall group delay experienced by both paths will be balanced, that is, virtually the same. This is an important aspect of having a symmetric collinear autocorrelator.

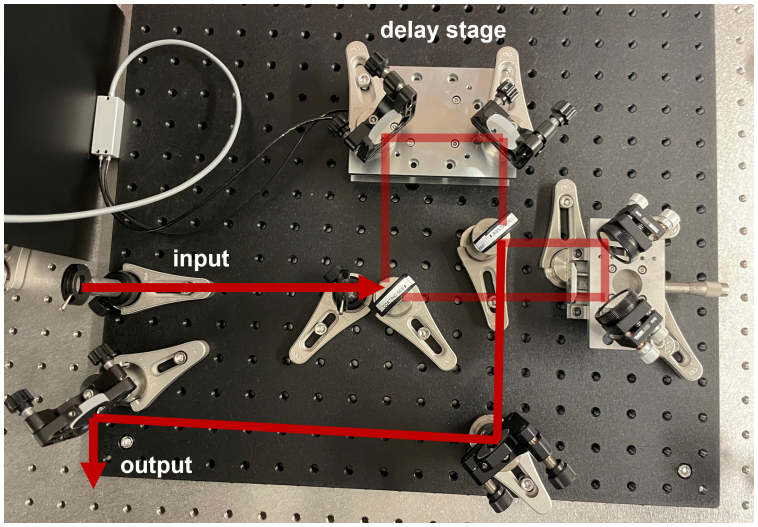

Figure 4-5: **Autocorrelator** - This setup consists of a piezo-driven stage in one arm and a manually adjustable stage used for aligning the trace with the driving voltage used for the piezo.

Returning to the overall layout of our autocorrelator, one of the beam paths passes through a delay stage. Here, the highly reflective (HR) mirrors sit on top of a piezo-based linear stage providing 200 μm travel across one axis with nanometer precision (Newport NPX200-SG). This translation will consequently cause the beam traveling in this path to experience twice this length, yielding a total achievable delay of $2(200\mu\text{m})/c = 1.3$ ps delay in time.

The other beam path travels to a manual translation stage that remains fixed during measurement recordings, but can be adjusted to align the autocorrelation trace within the same voltage domain of the piezo-driven delay stage. As the piezo is driven by a triangular wave voltage, the peak and trough of this wave should correspond to the beginning and end (or vice versa) of the autocorrelation trace, with $\tau = 0$ occurring ideally when the delay

stage has reached half of its displacement. This ensures that the autocorrelation trace being recorded is not interrupted due to the delay stage reaching its full maximum or minimum distance. After propagating through the fixed stage, both beams combine at the second BS and are sent to another set of steering mirrors before reaching the last section.

In the last optical section, the collinear beams arrive at the chopper that modulates the signal at a programmed frequency for signal retrieval using lock-in techniques in the same manner as was previously described in subsection 3.3.5. The modulated signal is then focused by a LA1255-C plano-convex lens (Thorlabs) which has a focal length of 50 mm. The second harmonic generation crystal is placed right at the focal length of the PCL to start the SHG process. The birefringent crystal used is Beta-Barium Borate (BBO) that is 10 μm in thickness, AR coated, 6mm x 6mm in area, and cut for 1030 nm SHG (Shalom Electro Optics). As the diverging signals (both the fundamental and produced SHG) exit the crystal, they enter another PCL (Thorlabs LA1255-C) to be re-collimated again as shown in Figure 4-6.

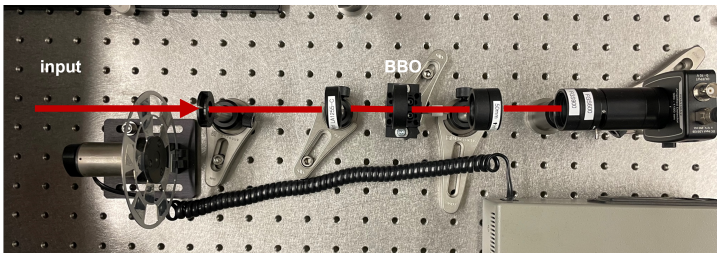

Figure 4-6: **Input to crystal** - Top view of an input beam progressing through the "chopper", PCL, BBO, PCL, two filters, and finally, the photodetector.

The two collinear beams now reach two colored-glass filters: FGS900 (Thorlabs), and FGS600 (Thorlabs), which have 85.79% transmittance at 550 nm (0.081% transmittance at 1100 nm), and 83.75% transmittance at 550 nm (0.034% at 1100 nm), respectively. The 550 nm is the second harmonic wavelength generated from the 1100 nm signal that went through the nonlinear crystal. In total, both of these filters allow 71.85% of the 550 nm beam to transmit and reach the detector, while only allowing 2.75 $\times 10^{-5}$% of the 1100 beam to pass through and reach the detector. Hopefully, this will virtually completely remove the infrared beam by giving a relative attenuation of 3.833 $\times 10^{-7}$%.

The last part of our beam path is the detector. For these initial tests, we used a

PDA100A2 amplified Si photodiode detector from Thorlabs. (We intended to use our custom-built, high-gain TIA system after initial testing.) The output of this detector is sent to a lock-in amplifier. The lock-in amplifier (Stanford Research Systems SR830) finds the modulated (chopped) signal among a sea of noise by applying a bandpass filter at the center frequency of our chopper (our modulation frequency). As we will see, it seems that the attenuation of the infrared was not sufficient. At the detector, our modulated SHG signal is not the only radiation that we observe. We also see the fundamental infrared pulse.

4.1.2 Interferometer Alignment

Proper alignment is crucial in any optical experiment. However, alignment is particularly critical in experiments where you want to interfere two beams in both space and time. For alignment in our system, steering mirrors are placed in strategic positions that allow walking the beam in virtually any direction. A beam can stray off an assumed parallel path if, for example, the laser source is not leveled, or some mirrors decide to tilt down for a day.

The alignment process requires two steering mirrors and two irises. The farther apart the two iris are, the better aligned the beam will be relative to other mounted components. Steering mirrors have two knobs attached to them. One controls the azimuth angle, while the other controls its altitude angle (often referred to as the angle of elevation). The beam is considered aligned when it goes through the center of both irises when they are tightly closed. The phrase "walking the beam" is used to describe the iterative process of slowly converging to the center of both irises. As this iterative process is performed, a visible beam would appear to be waltzing around the iris until finally converging on the center aperture. In our case, however, the fundamental beam is outside the visible spectrum, making this iterative process a bit more challenging and tedious.

Nevertheless, the first steering mirror controls a great deal of sway on the position of the beam while the second controls small increments in angle displacements. For this reason, the first steering mirror is first aligned to the first iris ("position alignment"), while the second steering mirror corrects to the second iris ("angle alignment"). As the second steering mirror is moved, the beam consequently becomes misaligned to the first iris, but not substantially. The first iteration is complete and so the first steering mirror aligns to the first iris again

and so on, until a proper alignment is reached.

In our interferometer, the alignment process involves, not just overlapping a beam to a set of irises, but overlapping to beams in space. The beams in the two different paths through the interferometer must fully overlap over each other. Additionally, these beams consist of pulses, and these pulses must overlap in time; so, the lengths of these two paths must be nearly identical. To achieve such precise spatial and temporal alignment, a detector array that can map out the pulse replaces our detector. This "camera" enables us to visualize the beams overlapping in space. Additionally, when spatial interference patterns appear on our camera display, we know that the beams must overlap in time (although they are somewhat misaligned in space). Using this camera, we can bring the beams into temporal overlap and then fine tune our steering mirrors to ensure that the beams perfectly overlap in space. After a comprehensive alignment, a single spot should appear on the camera, and when the delay between the two arms is tuned, this spot should disappear (complete destructive interference) and then reappear (complete constructive interference). High contrast between the destructive and constructive interference points confirms that we have excellent alignment in time and space. In Figure 4-7 we show an example of destructive and constructive interference exhibiting a well-aligned autocorrelator.

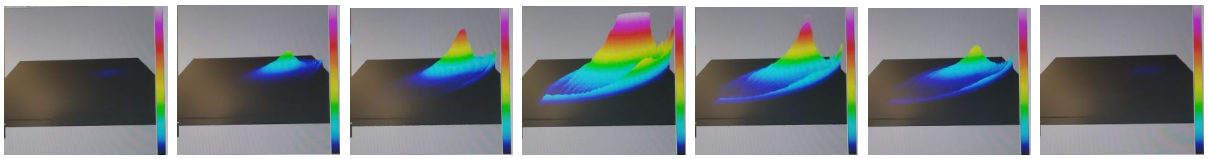

Figure 4-7: **Alignment** - These figures were taken from a video recording that shows a frame-by-frame visual of the beam profile showing deconstructive and constructive interferences.

4.1.3 Initial Results

After complete alignment of our autocorrelator, we made initial measurements. In Figure 4-7, we present a representative initial measurement. We should note that in this initial measurement the vertical axis is arbitrarily normalized. Additionally, the horizontal delay axis is also normalized. (In recording this data trace, we accidentally did not save the data corresponding to the strain gauge reading of the piezo; in other words, we did not save

the exact time axis data. The piezo displacement over the autocorrelation is approximately linear; however, we unfortunately do not have exact time data to present in this figure.)

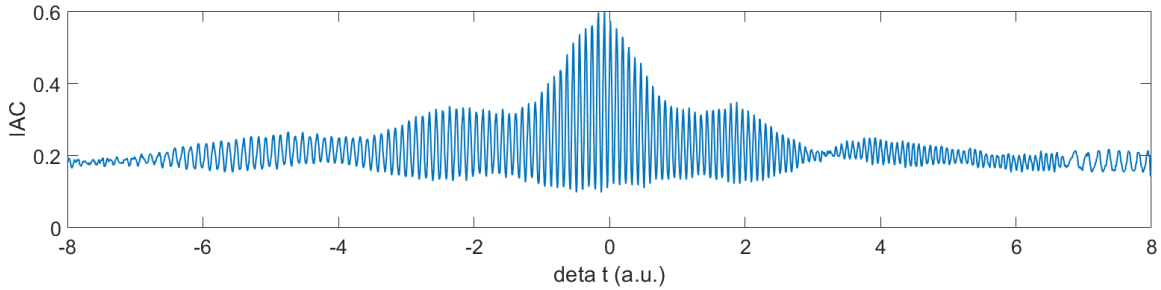

Figure 4-8: **Initial IAC trace** - Two major issues can be spotted at first glance: First, The trace is asymmetric. Second, the ratio is not 8:1. Although this is not a good measurement, we can learn from this by analyzing what could have gone wrong.

The initial results show some unexpected features. First the trace is asymmetric. Considering the mathematical form of the autocorrelation, we should always expect a symmetric trace. At first, we attributed this asymmetry to misalignment. However, even with excellent alignment (confirmed by our camera), this asymmetry persisted. Next, we can note that the signal-to-background ratio expected for an interferometric autocorrelation is incorrect. The minimum value of the trace is approximately 0.1 (in our arbitrary, normalized units). This puts the background level at $0.2 - 0.1 = 0.1$, and the signal-to-background ratio is approximately 6:1, not 8:1, as expected. Lastly, and most telling, if we inspect the period of the constructive and destructive interference fringes, we find something very interesting: this period corresponds to a central optical wavelength of approximately 1100 nm. This is the infrared wavelength of our fundamental light.

From the above analysis, we conclude that in our initial measurements, we have infrared light corrupting our result. Our colored-glass filters must not present sufficient attenuation. The SHG from our very thin BBO crystal is weak enough that even the small amount of infrared leakage through our filters can overwhelm the interesting SHG signal. The competition between the infrared light and the interesting SHG signal likely leads to the asymmetric autocorrelation trace, the irregular signal-to-background ratio, and the incorrect fringe periodicity. In the following section, we will describe how we aim to improve this pulse measurement strategy and what our next steps will be.

4.2 Next Steps - Intensity Autocorrelation

In the preceding section we discussed the layout, alignment, and measurements of an interferometric autocorrelator. We had elected to develop an interferometric autocorrelator as, among the basic autocorrelator types, these autocorrelators provide the most information about the measured pulses. However, as we saw in the previous section our interferometric autocorrelator is currently unable to separate the fundamental infrared wave from the relevant SHG signal. In this brief section, we describe how we can overcome this limitation, and we present a short outline of the next steps that we will take to measure our second harmonic pulses from our Cr:ZnSe/S laser.

Considering our interferometric autocorrelation, the solution to our challenge seems straightforward: use further filtering to eliminate the fundamental infrared signal. However, this solution may prove inadequate. The initial results presented were already approaching the limits of our detection capabilities. The detected signal was exceptionally weak. If this signal is larger than the SHG signal of interest, then even if we are able to separate our SHG signal from the fundamental light, we may still not be able to make the high signal-to-noise measurements that we desire. So, beyond the need for better filtering of the fundamental, we also need higher overall signal.

A logical solution to both problems described above is intensity autocorrelation. First, let us consider filtering, in the intensity autocorrelator our fundamental light will enter our BBO crystal at an angle (see Chapter 2). The resulting SHG will travel in a different direction than our fundamental light. Therefore, we can easily use an iris or aperture to filter out the fundamental light. This spatial filtering can provide enormous and tunable attenuation. Now let us consider the problem of overall signal. As described in Chapter 2, the intensity autocorrelator only requires one beamsplitter. Fundamentally, the intensity autocorrelator can use a shorter beam path and will always use the full power of the incident beam to generate SHG. Overall, we anticipate that these beneficial structural characteristics of the intensity autocorrelator will enable us to achieve higher signal. One last advantage of the intensity autocorrelator is its extend-ability. After initial pulse measurements, we aim to do more complete characterization of the second harmonic pulses from our Cr:ZnSe/S laser.

Specifically, we aim to build a frequency-resolved optical gating (FROG) system for complete retrieval of the group delay of the pulses. The intensity autocorrelator can be extended into a FROG system in a direct and straightforward way and will therefore make an excellent platform for future work.

Overall, in conclusion, in this thesis we have developed precision electronics and optics for the measurement of ultrafast, second harmonic laser pulses from a Cr:ZnSe/S laser system. We have characterized the electronics and optics, and we have presented initial pulse measurements. Due to time constraints, we were unable to completely connect all of our developments; we were unable to use our high-gain, low-noise TIA for pulse measurements in an intensity autocorrelator. However, we made significant progress developing these tools an setting up future researchers to complete these measurements and perform the first characterization of these intriguing second harmonic pulses that are naturally produced in Cr:ZnSe/S lasers.

Bibliography

[1] Sergey Vasilyev, Igor Moskalev, Viktor Smolski, Jeremy Peppers, Mike Mirov, Yury Barnakov, Vladimir Fedorov, Dmitry Martyshkin, Sergey Mirov, and Valentin Gapontsev. Kerr-lens mode-locked cr:zns oscillator reaches the spectral span of an optical octave. *Opt. Express*, 29(2):2458–2465, Jan 2021.

[2] Sergey Vasilyev, Igor Moskalev, Mike Mirov, Viktor Smolski, Sergey Mirov, and Valentin Gapontsev. Mid-ir kerr-lens mode-locked polycrystalline cr:zns and cr:znse lasers with intracavity frequency conversion via random quasi-phase-matching. *SPIE LASE*, page 97310B, 03 2016.

[3] Sergey Vasilyev, Igor Moskalev, Mike Mirov, Viktor Smolski, Sergey Mirov, and Valentin Gapontsev. Ultrafast middle-ir lasers and amplifiers based on polycrystalline cr:zns and cr:znse. *Opt. Mater. Express*, 7(7):2636–2650, Jul 2017.

[4] S. Choundhary and R. W. Boyd. *Tutorial on Nonlinear Optics*. IOS, Amsterdam; SIF, Bologna, 2016.

[5] Andrew M. Weiner. *Ultrafast Optics*. Wiley, 2009.

[6] Christian Spielmann, Lin Xu, and Ferenc Krausz. Measurement of interferometric autocorrelations: comment. *Applied optics*, 36(12):2523–2525, 1997.

[7] PLANAR DIFFUSED SILICON PHOTODIODE. Photodiode characteristics and applications.

[8] Donal Neamen. *An Introduction to Semiconductor Devices*. McGraw Hill, 2006.

[9] S1223-01 datasheet. `https://docs.rs-online.com/ec2b/0900766b80d838f0.pdf`. Accessed: 2022-11-18.

[10] Burr-Brown Corporation. Noise analysis of fet transimpedance amplifiers. *Application Bulletin*, AB-076:1–5, February 1994.

[11] Ltc 6241hv datasheet. `https://www.analog.com/media/en/technical-documentation/data-sheets/624012fe.pdf`. Accessed: 2022-11-18.

[12] Pingqiang Zhou. *Laboratory manual for Introduction to Circuits and Instruments*. ShanghaiTech University, 2015.

[13] Philip CD Hobbs. Photodiode front ends: The real story. *Optics and Photonics News*, 12(4):44–47, 2001.

[14] Ray optics simulation. `https://www.falstad.com/ray-optics/simulator/`. Accessed: 2022-11-16.